CUSTOMIZATION OF MEMS BASED HYDRAULIC PRESSURE SENSOR

A Thesis

Submitted

In Partial Fulfillment of the Requirements

For the Degree of

MASTER OF TECHNOLOGY

In

Production and Industrial Engineering

Submitted by

Sanjay Kumar Ghoshal

Under the Supervision of

Mr. Yaqoob Ali Ansari

Assistant Professor

Department of Mechanical Engineering

Faculty of Engineering

INTEGRAL UNIVERSITY,LUCKNOW,INDIA

June,2022

CERTIFICATE

This is to certified **Mr. Sanjay Kumar Ghoshal** (Enroll. No.-1900102392) has carried out the research work presented in this thesis **"CUSTOMIZATION MEMS BASED HYDRAULIC PRESSURE SENSOR "** submitted for partial fulfillment for the award of **Degree of Master of Technology in Production and Industrial Engineering** from **Integral University, Lucknow** under my supervision .thesis embodies results of original work, and studies are carried out by the student himself and the contents of the thesis do not form the basis for the award of any other degree to the candidate or to anybody else from this or any other University/Institution.

Signature of Supervisor

Full Name: **Mr. Yaqoob Ali Ansari**,

Designation: Assistant Professor,

Department of Mechanical Engineering

Integral University, Lucknow.

Date:

Place:

DECLARATION

I hereby declare that the thesis titled "**CUSTOMIZATION MEMS BASED HYDRAULIC PRESSURE SENSOR"** is an authentic record of the research work carried out by me under the supervision of Mr. **Yaqoob Ali Ansari Assistant Professor, Department of Mechanical Engineering, Integral University, Lucknow**. No part of this thesis has been presented elsewhere for any other degree or diploma earlier.

I declare that I have faithfully acknowledged and referred to the works of other researchers wherever their published works have been cited in the thesis. I further certifythat I have not willfully taken other's work, text, data, results, tables, figures etc.reported in the journals, books, magazines, reports, dissertations, theses, etc., or availableat web-sites without their permission, and have not included those in this Master of technology. Thesis citing as my own work.

Date: Signature: _____

Name:**Sanjay Kumar Ghoshal**

Enroll.No:**1900102392**

ACKNOWLEDEMENT

First of all I am highly indebted and thankful the almighty god the most merciful and benevolent to all, who taught me that which he knew bestowed the men with epistemology and gave him the potential to ameliorate the same. It is my pleasant duty to acknowledge the help received from several individuals during the work.

I wish to express my profound gratitude, respect and honor to my supervisor **Mr. Yaqoob Ali Ansari, Assistant Professor, Department of Mechanical Engineering, Integral University Lucknow**, for their illuminative and precious guidance, constant supervision, critical opinion and timely suggestion , constant useful encouragement and technical tips which has always been a source of inspiration during the preparation of dissertation.

I would also like to thank the rest of dissertation committee, **Prof. Dr. Prem Kumar Bharti (HOD) Department of Mechanical Engineering ,** my dissertation **Incharge Dr. Mohd Anas Associate Professor,** Entire Faculties and staff of **Department of Mechanical Engineering** for their supports, encouragement and providing me the opportunities while working on this exciting research.

I will be failing in my duties if I miss to express my profound and deepest sense of gratitude to my beloved parents and other members of family and friends for their keen interest in my studies, immense support and encouragement , without which it was impossible to complete this dissertation.

I also place on record my sense of gratitude to one and all who directly or indirectly. Have lent their hand in this thesis.

Date: Signature: _____

Name:**Sanjay Kumar Ghoshal**

Enroll.No:**1900102392**

TABLE OF CONTENTS

LIST OF TABLES

LIST OF FIGURES

ABSTRACT

In the literature tuning forks are used for measurement of the deflection of a diaphragm. However, in this study, a tuning fork is configured to lay in orthogonal direction with a diaphragm of which centre point deflection is being measured. Upon application of pressure, centre deflection of the diaphragm induces an axial compressive load on the DETF resonator which induces decrease in natural frequency of the resonator. Since the tip is vulnerable, a roller structure which is simply a guided beam is included in the design to protect tip from transverse components of measured displacement.

Additionally, the applied displacement is directed through the roller to a spring element which transmits nearly 1 % of tip displacement to DETF. Although the addition of the spring adversely affects the sensitivity, the spring increases the overall compliance of the tip which increases the assembly yield.

Advantage of such design is that by modifying the geometry of the spring or the diaphragm, different pressure ranges for measurement can be attained. The resonator's tine dimensions are optimized for maximum of sensitivity quality factor product. The device can operate in atmospheric conditions, and hence the design makes use of overlapping comb fingers to avoid squeeze film damping.

A pressure port is designed to keep diaphragm and MEMS sensor together in contact. The pressure port combines the deflection performance of aluminum for better sensitivity, and greater strength of steel for larger safety factor. Aluminum and steel parts are fixed together with interference fit for demonstration of the sensor operation In this study measurement of pressure relies on use of diaphragm and strain sensor similar to many other publications. But this

dissertation offers a novel. Being distinct from other studies, diaphragm and resonator is not in parallel position. Instead, resonator is positioned orthogonally with respect to diaphragm. By using this property design can achieve higher resolution in a broader range. Moreover this property enables design to work with different diaphragm geometries without modifying the MEMS component.

Plane of work Outline:

1. Double ended tuning fork (DETF) optimization of the design.
2. Design of pressure port and other supplementary structures.
3. Fabrication of sensor core and pressure port .

Test results of the devices which have the optimized geometry are demonstrated. Along with these results, detection setup and assembly of the sensor with pressure port is described. Tests are performed in three types. First the working devices are determined and separated with resonance tests. The resonance tests are conducted with probe station without taking electrical connections by means of wiring. Secondly, displacement tests are performed with working devices by using a precise piezoelectric actuator

CHAPTER 1

INTRODUCTION

The development of micro gadgetry has increased significantly over the years, leading to their widespread usage as modern tools for humans. During this period, it became simple to have access to a tremendous amount of knowledge about the universe. Despite the fact that we've got enough about the Earth, new drones are being deployed into outer space to collect data. Some people, though, are considering mining the moon. Nobody tries to land on the moon nowadays. Information is limitless, but obtaining it takes time and is difficult, therefore it dictates our speed. It's crucial to remember that tests and measurements to be used in this circumstance to gather and validate information. Smaller devices are better measurement tools, which is why they've gained popularity and been accepted by plenty of individuals.

MEMS gadgets are right now the most predominant sort of little device. They are dynamic, seeing, and impelling, and they are all over the place. One such delineation of a tactile application is a clock. Despite the fact that quartz is a brilliant watch, most current timekeepers utilize MEMS resonators since they are more reasonable and clearer to make. Silicon and MEMS have been utilized in various gadgets beginning around 1982, when silicon was at first proposed as minimal in excess of a specialist material [1]. These gadgets differ from clocks to satellite drive [2]. Regardless of whether subjects like microscale peculiarities and the utilization of silicon as a material have gone through broad examination, there are as yet various tests accessible where data is simply ready to be revealed.

This research, like many others, uses a diaphragm and even a strain sensor to detect pressure. This dissertation, on the other hand, is unique. In contrast to past findings, because resonance as well as diaphragm weren't in the same plane. Instead, the resonator is positioned orthogonally to the diaphragm. Design can boost resolution across a wider range by using this attribute. This trait enables the system to be flexible without altering the MEMS component and accommodate various diaphragm forms.

1.1. Dissertation Outline

The exposition's blueprint begins with a concise presentation in the primary section determined to convey motivation by means of the essentials of the plan, forthcoming application regions, and a survey of the writing of relevant exploration. The subsequent section investigates the plan interaction's directing belief system. This' part will likely depict how this thought will be carried out. The recurrence shift peculiarities for a tuning fork development are in this way originally examined. The quality variable evaluation, one of the main components to consider while picking a plan, is then interpreted. The third section makes full use about the twofold finished tuning fork (DETF) streamlining plan subtask. In any case, it likewise incorporates the making of a tension port and other help structures. The third section means to consolidate data with top to bottom examination. Following that, the fourth segment gives insights concerning how the sensor center and water port are made. The fifth part talks about the portrayal of the gadgets as well as the outcomes. At long last, the review's results are summed up and closing notes are given in the part on future comments and discussions.

1.2 Design Basics of the Hydraulic Pressure Sensor

One advantage of the plan is the utilization of a DETF resonator. These resonators have phenomenal mechanical strength. They can keep on working while at the same time being encircled by resounding recurrence despite everything hold their mechanical abilities. Furthermore, their hysteresis is negligible [3]. As a result of these two qualities, DETF has high steadiness, yet it likewise upgrades responsiveness since it needn't bother with an enormous confirmation mass.

The plan offers a huge unique scope of activity since it joins two parts, a strain port and a MEMS resonator. All the more explicitly, to achieve higher tension restrictions, the pressure port component can be changed while the resonator part is left unaltered. It would be ideal for it to be referenced that the strain sensor utilized in this review was tried at a most extreme tension of 60 bars.

This tension is far under 10 m when it is converted into relocation by the plan's stomach.

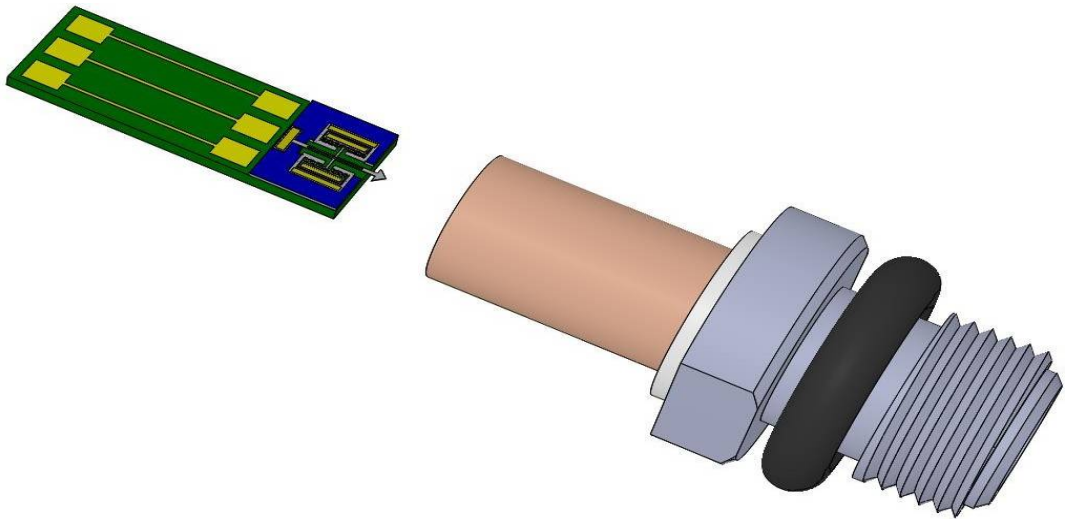

Be that as it may, DETF is made to endure 100 m of hub pressure without clasping thanks to a series of spring parts. Subsequently, resonator parts may promptly be matched with more many-sided pressure port sorts that can endure applications with more prominent tension.

Resonator tip and stomach should be in nearness to each other. Subsequently, assembling the sensor's parts is a significant stage when DETF is in danger of being hurt. The DETF design's insurance against shocks is the primary motivation to set the pivotal pressure limit at a high worth. High pivotal pressure limit makes it less likely that mistakes made while assembling the construction's pieces could cause harm. Thus, the sensor's strength is improved. The capacity of the proposed sensor to work at climatic tension but get adequately top notch factor values is a fundamental measures. For MEMS resonators, vacuum activity is in many cases the favored situation. This is because of the energy scattering and potential spring capability of the air that occupies the spaces in microstructures. Thus, the design's quality component declines, bringing about less responsiveness and a requirement for more info ability to work the framework at reverberation. Notwithstanding, the development and testing of the gadgets are troubled somewhat by working in vacuum. Furthermore, specifically, it is trying to keep up with bundle level vacuum for a strain detecting component that must precisely contact with the external climate at its tip. Subsequently, notwithstanding endeavoring to meet high standards A printed circuit board is utilized as a halfway stage for electrical associations. The board's opposite end is utilized to eliminate the wires, while its opposite end is utilized to introduce the resonator.

The resonator's electrical associations are laid out with a wire bonder, and the wires are welded. On the board, there is a void space between two arrangements of cushions, diminishing the chance of a MEMS gadget coming into close contact with bubbling weld.

The goal of the proposed sensor design is to detect high hydraulic pressures. The resonator's huge maximum deflection limit is dynamically given for this. There are several industrial application areas that need for high hydraulic pressure. A quick explanation of these locations and how the provided sensor may be used will be provided in this section.

Hydroforming of malleable metals is one of the essential purposes for high water driven pressure, which is fundamentally attached to the modern business. In this creation technique, metal sheet is taken care of into a pass on. From that point onward, pressure driven liquid is infused into the area where metal will create. The need of assessing inner strain originates from process factors, since disappointments, for example, kinks may be seen beyond a predetermined period [4]. Notwithstanding kick the bucket framing, drawing methods are being applied through hydroforming. This strategy is comparatively reliant upon the liquid's strain since the p The drawing pace of the metal, which is a critical viewpoint in the activity's exhibition, is pressure subordinate [5]. This technique applies water driven strain to the catapulting locale to accomplish a certain darting pre-stress. The two packed materials are then clasped together by just pivoting the bolt. Better exactness is gotten when a bolt is tensioned powerfully, and how much strain for this approach is contrarily corresponding to water driven pressure. Accordingly, the strategy's advancement of precision is intently attached to it.

Pressure affects the stretching rate of the metal, which is essential for fruitful activity [5]. Catastrophic self-warning frames are one of the interesting applications of sensors. In reality, the details of these frameworks are not completely met. Sensor types that meet the exhibition's recommended plans have recently been welcomed as progress towards that goal [6]. Relevant plans remain hidden in the area of written exams for a long time, but it is important to note that these reminder frameworks require more developed print targets. In an ongoing investigation, a pair of sensors, one of which is a hydraulic pressure sensor, will be launched to the surface of the sea. Estimates of surface pressure are made at 6000 meters above sea level or less than about 600 bar. Several distant waves are observed before the evaluation is made. Later, these

sensors will be used in Japanese DONET research [7]. High voltage targets make it easy to detect seismic impacts from waves. Prior to the widespread use of autofrettage processes aimed at extending the useful life of cylinder parts, high stresses of, for example, 1000 bar were regularly used [9]. In the automotive field, fuel injection systems are commonly deployed using this strategy. This approach applies compressed weight to the internal mass of the cylinder by applying tension to the cylinder. This residual stress allows professionals to extend fatigue life without widening the outer width or using additional materials.

CHAPTER 2

Literature Review

In this section resonant pressure sensors are reviewed in detail first. Then example sensor applications of DETF resonators are investigated.

2.1. Resonant Pressure Sensors

Pressure sensors are available in a wide range of structural configurations, detection and actuation techniques for a variety of areas and applications. One such application-specific design is an optically driven MEMS pressure sensor aimed at having a wide range [10], the purpose of which is harsh while measuring single point pressure from a fiber cable. To withstand the conditions. It claims to have a low linear drift of 250ppm and a wide measurement range of 0-206bar, but it lacks sensitivity at 0.13Hz / kPa. There are also highly sensitive options, such as the touch-mode capacitive pressure sensor provided by Fra Giacomo [11]. The maximum sensitivity of this type is given by the sensor shown as 14 pF / bar. However, the authors claim that there are drawbacks such as hysteresis, process reliability issues, and advanced conditioning electronics. Also, there is no full scale from 0 to 10 bars. In addition, piezo resistance pressure sensors are widely used on the market due to their low cost. These are highly compatible with IC technology and can be obtained through a variety of basic clean room operations [11]. In addition, piezo resistance provides outstanding linearity [12, 13]. However, the inevitable temperature drift [14] and the inadequate sensitivity of this efficient approach [15] have drawbacks. However, the inevitable temperature drift [14] and the inadequate sensitivity of this efficient approach [15] have drawbacks. Resonators, on the other hand, have significant advantages over capacitive and piezo-resistant cousins. Their outputs can be quickly captured and digitized with inexpensive frequency counters and easily integrated into capture electronics [16]. In addition, electrical noise and drift are minimal concerns for resonators, as the natural frequency of the resonator is only affected by shape and mechanical factors other than temperature [17]. This provides long-term stability compared to other methods. In addition, resonators are superior in terms of sensitivity [18]. The disadvantage of silicon resonators is that they are easily damaged by improper packaging conditions and other manufacturing residual stresses [19]. Nevertheless, the proposed dissertation design does not

require packaging and does not have a difficult and stressful manufacturing process. As a result, the resonator appears to be optimal for operation. There are several resonator devices used to measure pressure in the literature. Most of these devices contain resonators that are parallel to the diaphragm. Ren and Welham have described extremely simple instances of such designs that are similar [20, 21]. In Figure 2.1, the corresponding tuning forks of two investigations are displayed. Both investigations used comb fingers for drive and sensing electrodes, with natural frequencies of 35 and 52 kHz, respectively.

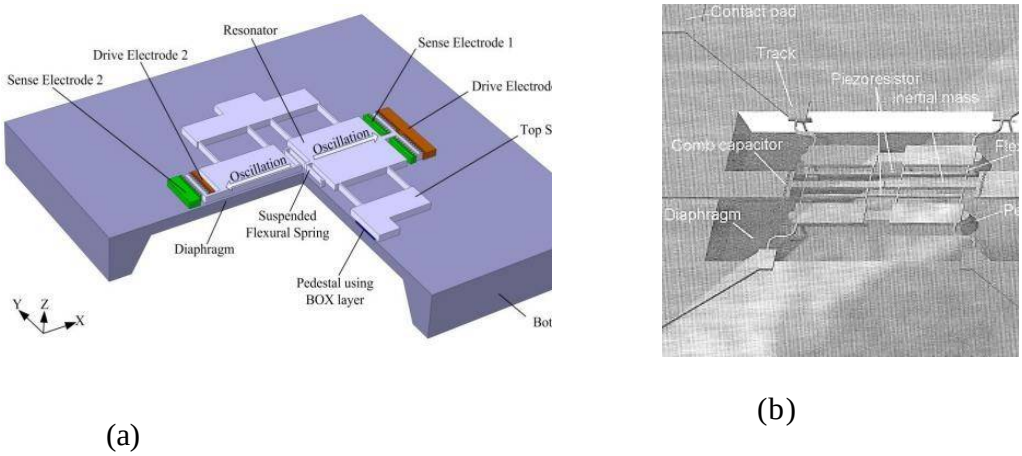

(a) (b)

Figure 2.1 - Illustrative view of two similar simple methods adopted by early researchers. (a) Fabrication view of DETF on a diaphragm from [20] and (b) fabricated view from [21]

Since both studies are aimed at operating the device under atmospheric conditions, the given quality factor for the two experiments is about 1000. Measurements are made at intervals of 0-6 and 0-10 bar, respectively. These two articles show one of the most basic ways to measure pressure using a resonator. In contrast to using comb fingers or the electrostatic method, an alternative technique above design is provided by electromagnetically resonating the resonator [22]. Compared to previous studies, this reports a range of 0-1 bars at a resolution of 10 Pa. The sensitivity of the device is about 6 times higher than in previous tests at 122 kHz / Pa.

BO proposed to use a concept similar to tuning forks, but under vacuum [23]. In the Bo design shown in Figure 2.2, wafer level packaging and capacitive plates were used for the sense and drive electrodes instead of comb fingers, as reducing film damping is not a problem for devices operating in vacuum. As a result, this study yielded an extraordinary quality factor of about 10,000 after months of operation. Despite this, the reported sensitivity of 166 Hz/kPa

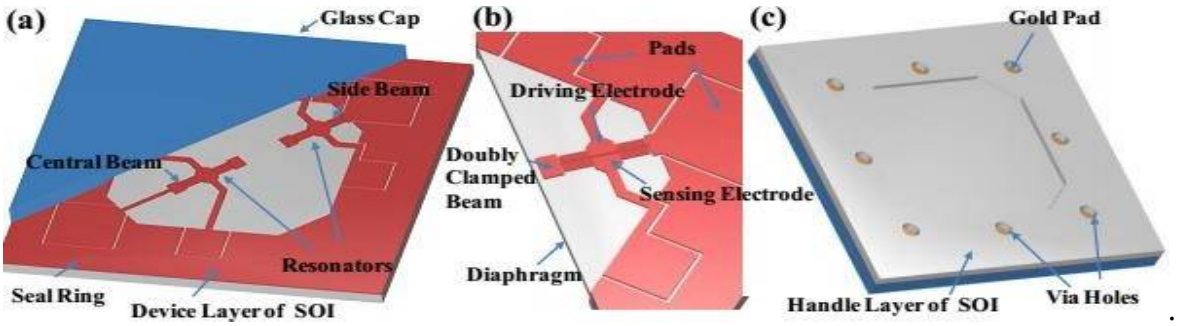

Figure 2.2 - Cross sectional and packaged view of a wafer level vacuum packaged pressuresensor [23]

Kinnell's 2009 study claims a system designed to operate under vacuum [14]. Figure 2.3 shows a cross section of the design. The importance of this design is comparable to the device proposed in the paper, high dynamic range. Kinnell uses a plate resonator instead of a tuning fork, but the dynamic range described is very similar. Fusion bonding is used for vacuum packaging, and some examples have a quality score of 35,000. Sensitivity and scaling are given as 30 Hz / kPa or 0-2 bar. It is also mentioned that the general flow of the manufacturing process increases the dynamic range of the device.

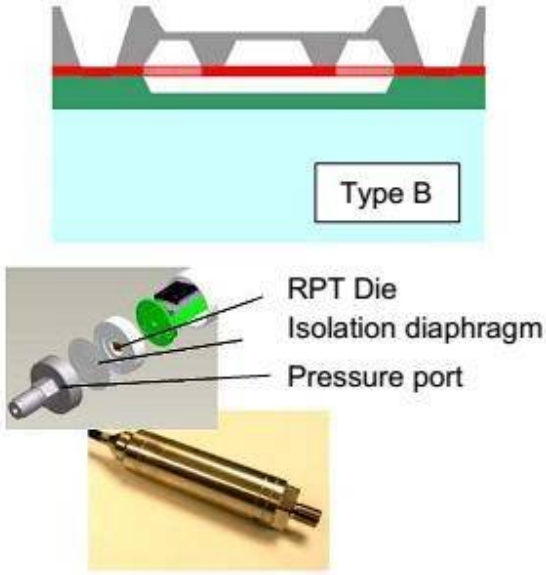

Figure 2.3 - Cross section view of a design proposed to have a high dynamic range of operationin hydraulic oil [14]

Although it is not explicitly specified, it is likely that diaphragm thickness is altered during production. The dissertation also mentions adjusting the diaphragm thickness for this reason.
So far, all the designs mentioned use resonators that work parallel to the membrane design. The main advantage of such a system is its ease of manufacture. Since the membrane can be easily manufactured in a clean room like a resonator, silicon can be used as the membrane material, and its excellent mechanical properties help in the design. However, the cost is small because the DETF structure cannot be loaded until it is twisted in parallel. Currently, there is only one design in the literature that claims to use the DETF structure at orthogonal to the diaphragm. It is the most notable device to date, nominated for a breakthrough product [6] and has extremely high resolution (10 ppb). There are three important differences between this and the proposed design. The first is the type of stress they are dealing with and the second is the material used. Older designs used quartz under tension, but the proposed concept uses silicon under pressure, which makes it more sensitive. The third difference is that this design uses the Bourdon tube shown in Figure 2.4 instead of the diaphragm.

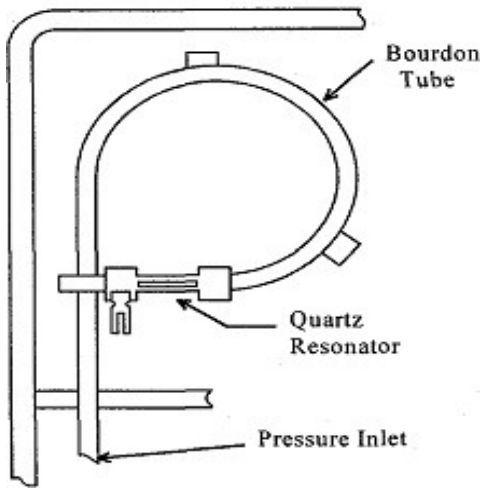

Figure 2.4 - State-of-the-art MEMS resonator pressure sensor obtained by using Bourdon tubeinstead of diaphragm [24]

2.2 Double-Ended Tuning Fork Sensor Applications

Compared to other types of resonators, DETF offers better detection quality. Properties such as low hysteresis and long-term stability make it easier for many researchers to understand why they are so widely used. In addition, the crystal DETF is widely used on the market and is partially suitable, reducing the manufacturing effort. Still, the two most important aspects of DETF are range and dissipative behavior. First, the DETF chip can be rotated until the range of the device is biased to point of immediate expansion. Second, unlike single-beam resonators, tuning forks have symmetrical characteristics. The two resonators are very weakly connected by an armature. In exchange for being a prong. As a result, DETF has opened many different application areas between sensors. As already mentioned, they are very sensitive to axial loads. However, their sensitivity depends on factors such as ambient volume characteristics, mass changes, and non-uniform vibrational energy localization, figures for understanding are shown, and operating principles are explained. The axial strain sensitivity mentioned above is used in several types of sensors. These include accelerometers, gyroscopes, magnetometers and more. Interestingly, however, many researchers use different principles in their work. The first example of this is that the moisture sensor used the dependence of the natural frequency on the mass of the resonator. An example has been proposed [25] and the proposed sensor has been reported to have high sensitivity, fast response, and good stability. This principle is derived by coating DETF tine with sol-gel to trap the moisture in the medium. This technique is very simple and easy to use. Another humidity sensor has been reported to operate under vacuum [26] and has an interesting operating principle. The proof mass electrode of this sensor is coated with silicon dioxide, and some of this oxide is open to the atmosphere. Higher ambient humidity reduces the resistance of silicon dioxide and accelerates the decay of charge from the proof ground electrode. Eventually, electrostatic spring softening term changes and frequency shift is observed.

Another very interesting sensor based on the silicon DETF structure is presented [27]. This sensor uses the difference in the localization of the vibration energy of DETF to measure the charge. In addition, it has been demonstrated that using this approach yields sensitivity values that are orders of magnitude higher at the cost of detecting frequency shifts. As shown in Figure 2.5, the two different resonators are very weakly coupled by the beam.

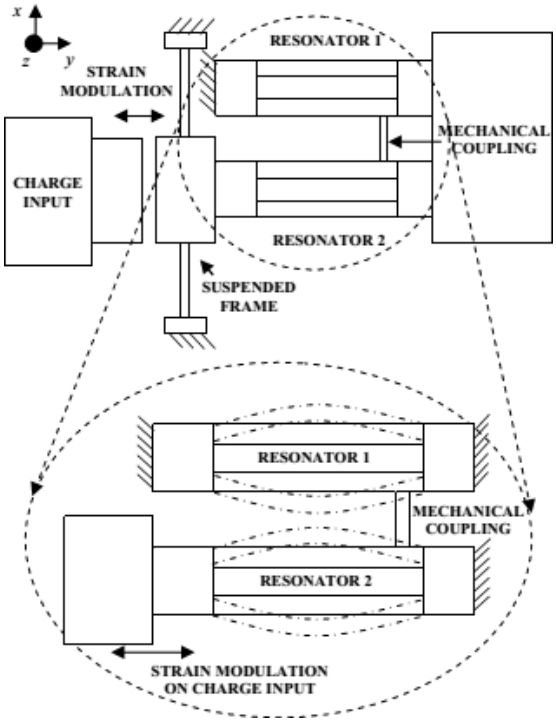

Figure 2.5 - Two resonators utilized for eigenvalue curve veering approach.

In this configuration, resonators 1 and 2 are indirectly and directly affected when loaded. Due to the perturbation of the Tyne of resonator 1, the DETF has an energy confinement region that changes its inherent state. This phenomenon, known as curve shear, provides a sensitive sensor. Apart from the application presented, researchers used DETF's axial stress sensitivity to build various sensors such as temperature, strain, torque, tilt, magnetic field, gyroscope, acceleration, and force sensors [28]. -35]. Some of these sensors are shown in the next part of this section. The temperature coefficient of Young's modulus of single crystal silicon has been shown to be about 60 ppm [36]. Therefore, the natural frequency of the resonator is actually directly affected by temperature. The use of this characteristic of a very stable silicon temperature sensor has been reported [28]. This is a very simple application of DETF, but when two resonators are used side by side, a temperature resolution of 0.16 mK and a relative frequency stability of 4.8 ppb are achieved. The torque sensor and strain sensor examined are almost the same [29, 30]. The resonator is fixed at both ends and is attached to the material of interest. Torque is detected by shear strain, but the strain sensor principle is based on the measurement of axial strain of a material.

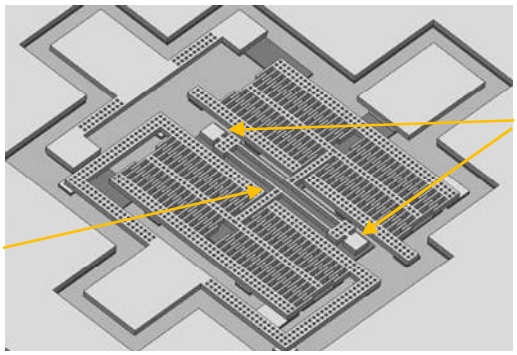

Figure 2.6- Double clamped DETF strain sensor [30]

You can get accelerometers and inclinometers by adding a proof mass and a DETF structure. Design of a 160Hz / g accelerometer with a proof mass between the sweatshirt and two other DETF resonators [31]. In addition, Zou documents a tilt sensor with an angular resolution of 500 nanoradians [32]. Both designs are shown in Figure 2.7. It turns out that the two designs are actually very similar in terms of cantilever, resonator, and proof mass placement.

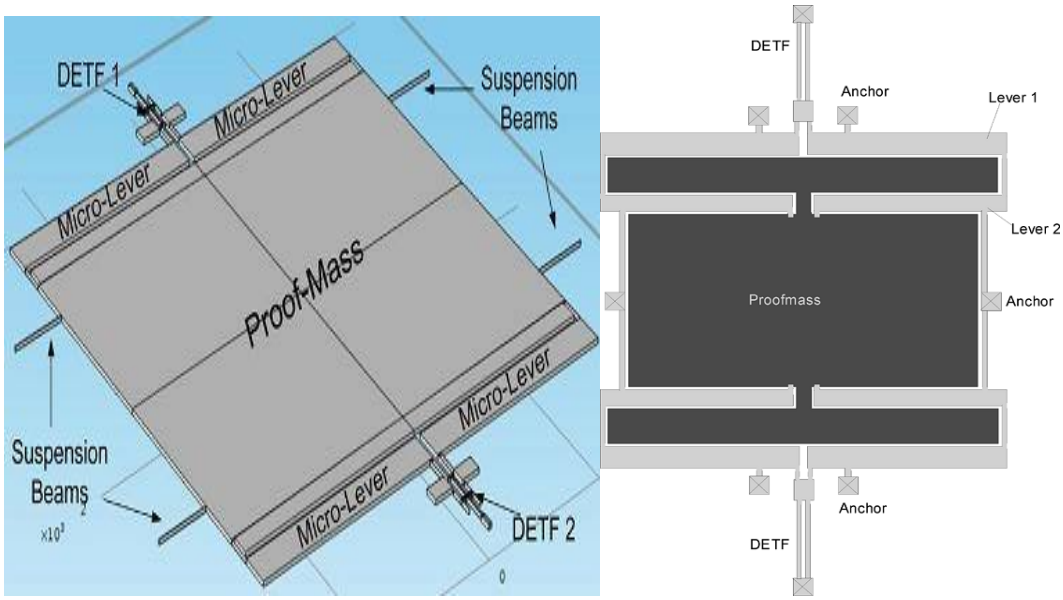

(a) b)

Figure 2.7 - Examples of DETF structures with proof mass addition, (a) a tilt sensor and (b) an accelerometer [32] [31].

In the case of the Zou tilt sensor, when the proof mass is exposed to the gravitational field on the vertical axis of the suspended beam, compressive stress is generated in one resonator and the other, as shown in Figure 2.7. Compressive stress is generated in the resonator. low voltage. Similarly, the accelerometer proof mass attempts to move vertically through the resonator when acceleration is applied. This movement of the proof mass is transmitted to a DETF resonator with a lever mechanism, during which the opposite type of voltage is generated. In another study, instead of a proof mass, the end of the DETF resonator was attached to a rod that absorbs Lorentz forces. [33] These crossbars and DETF alignment are shown in Figure 2.7 (a). When the rod is exposed to an out-of-plane magnetic field, the natural frequency of DETF shifts in the presence of axial stress. This study reports an ultra-high-quality factor (100,000) and a sensitivity of 215.74 ppm / day. In addition, with careful selection of device geometry, this sensitivity can be expected to be up to 10x higher.

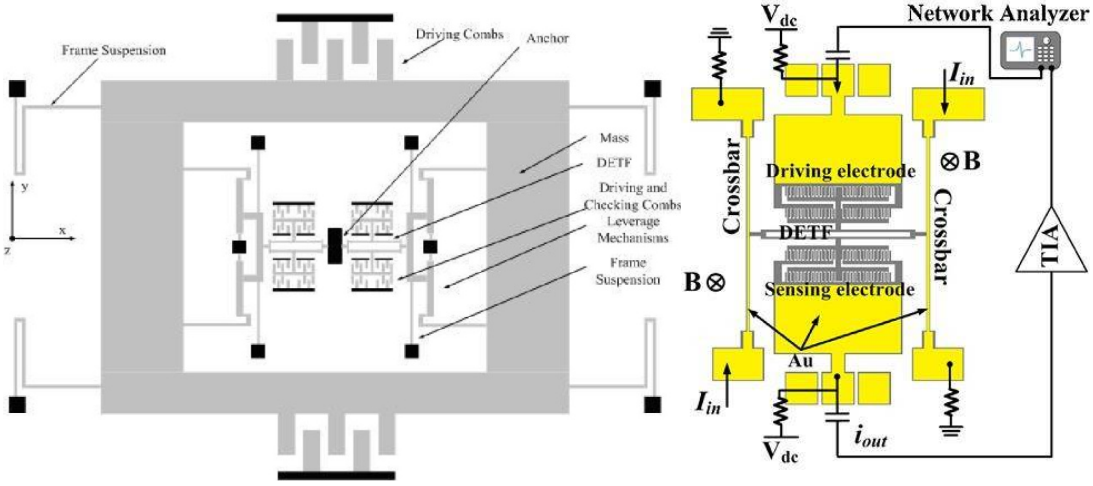

(a) (b)

Figure 2.8 - Two DETF resonators utilized with levers and an encircling proof mass for measuring rotation (a) a crossbar and magnetic field configuration of a DETF for measuring magnetic field (33); and (b) two DETF resonators.

The DETF structure, which serves as a gyroscope, is shown as the final example of its sort [35]. The movement of the mass m is magnified in this construction by use of levers. When a rotation is on an out-of-plane axis, Proof Masses experiences the Coriolis force. Last but not least, levers apply magnified motion to the longitudinal axis of two DETF resonators.

CHAPTER 3

THEORY OF RESONANT SENSING AND LOSS MECHANISM

The structure exhibits a large amplitude response at a particular excitation frequency, even at low excitation amplitudes. This phenomenon is called resonance, and the frequency generated is called the natural frequency ωn.In the absence of damping, natural frequency of a system can be defined .

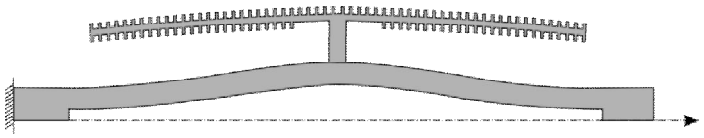

Figure 3.1 - Desired operational mode shape of DETF

According to the natural frequency of a system is determined by its mass and stiffness. You can now have a rudimentary understanding of resonance detection. The mechanical behavior of DETF structures made of two thin beams is especially examined in this paper, but is applicable to many different types of structures. The inherent frequency of the system changes when the beam's mass or stiffness increases. The latter decrease in stiffness serves as the foundation for the construction of this pressure sensor. The lateral stiffness of the structure is altered by axial compressive loads on the ends of the beam, particularly the tine, which lowers the resonator's natural frequency. Figure 3.1 displays the DETF's desired mode form as half of the structure. Figure 2 illustrates the required DETF mode shape. 1 at the center of the building. When seen in relation to the vertical axis, some other half is symmetric.

3.1 Theory of Resonant Force Sensing

As was already indicated, the application of an axial compressive force alters the stiffness of the tine. In this experiment, Tyne is a beam that is electrostatically induced to resonate. Furthermore, because the two DETF prongs are considered to have a symmetrical shape with respect to the vertical axis at resonance, only one prong is studied. The governing equation for such a beam's reaction is stated .

Where w is a function of axial position x and time t, and EI denotes flexural rigidity, Fapp stands for applied axial compressive force, for material density, and A for beam cross-section. The harmonic driving force acting laterally at the center of the beam is represented by the final P (x, t) term. This equation's first term describes the beam's flexural rigidity, while its second term adds tensile or compressive stiffness. The third term, which comes last, is the inertial force. A is the mass per period in that situation. At resonance, the modal form and modal coordinate terms, which are functions of x and t, respectively, are linked to the displacement w. Deflection can therefore be expressed as;

In above equation ϕ and q represents the mode shape and modal coordinate, respectively. For convenience $\varepsilon = x/L$ is defined and solution of the form is sought,

When (2.3) substituted into (2.2) effective mass and stiffness terms can be found as;

where mj and ε_j are masses and positions of capacitive plates at desired mode time shape. Mode shape function of a tine can be assumed as;

This function is driven geometrically from the shape of half of a tine at resonance itself which is shown in Figure 3.2.

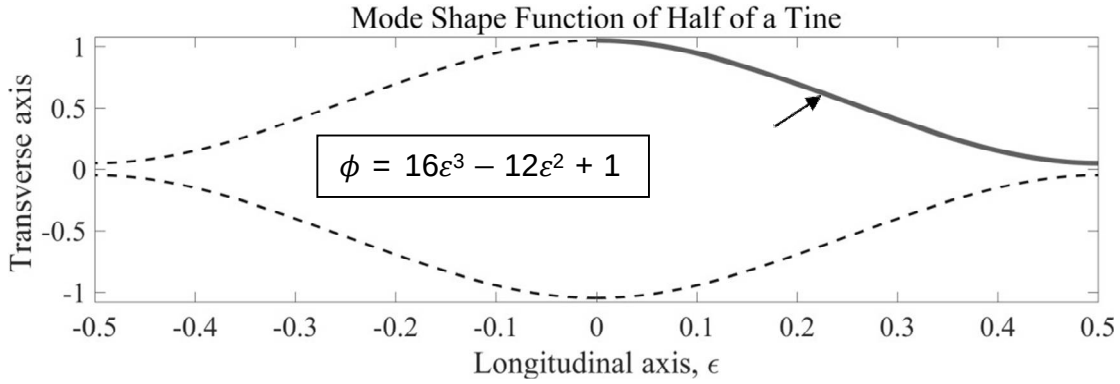

Figure 3.2 – Illustration of tines at desired resonance and corresponding mode shape functionfor half of a single tine

Half of the DETF is taken as a lumped mass and modal mass and stiffness can be found using (2.5) as follows;

where n_{comb} is the number of comb fingers;

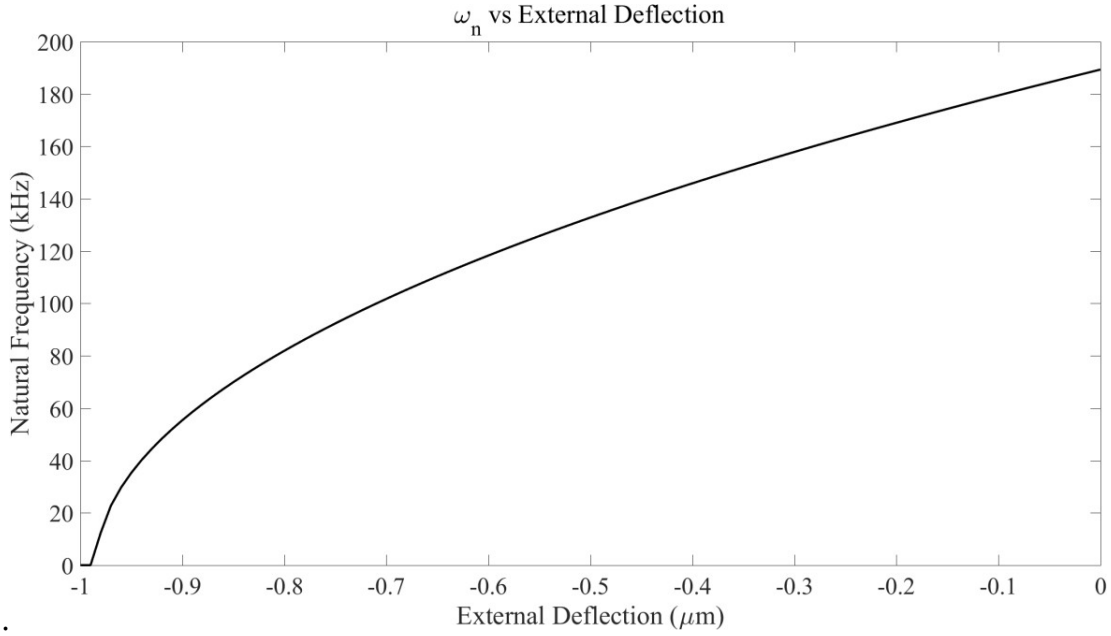

.

Figure 3.3 - Illustration of relation between axial load and natural frequency of a beam usingsingle degree of freedom model

After calculating such parameters, the problem of eigenvalues arises. However, the steps to fix this issue are described in Chap. 4. Meanwhile, this section presents the results of an

example problem to illustrate the frequency shift that accompanies the application of axial deflection. In this example, consider a simple ray with length, width, and height of 867 µm, 16 µm, and 35 µm, respectively. These dimensions actually correspond to the individual prongs of the DETF created in this study. The natural frequency of a beam of a given dimension can be found accurately using a single degree of freedom model. Therefore, by simplifying the integral we can calculate such a beam and substitute it find the natural frequency.

An illustration of the outcome of axial deflection at natural frequency is shown in Figure 2.3. It is important to keep in mind that negative axial deflection indicates the beam's effective stiffness and, consequently, the compressive force that lowers its natural frequency. Frequencies that reach zero with a deflection of around -1 m indicate a beam breakpoint. The natural frequency curve's slope is highest at this point, but the output voltage sensed by the capacitive plate is insufficient to provide an accurate reading in this frequency range. Around this point, sensitivity, i. H.

The ultimate Tyne reaction to an axial force can be demonstrated by considering a straightforward system with a single degree of freedom. The resulting frequency response gives an idea of what the sensor response will be like during the hydraulic test. For the single-degree-of-freedom system depicted in (2.4), the equation of motion is;

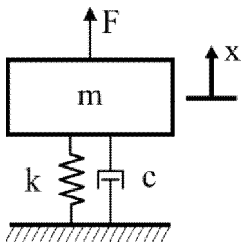

Figure 3.4 - Mechanical model of a single degree of freedom system

Then ratio of response to the forcing can be found as,Which is complex function and has a magnitude of finally by dividing both parts of right hand side of the equation by k, response can be written as Under deflection stiffness and hence natural frequency terms changes, which affects the response as shown in,

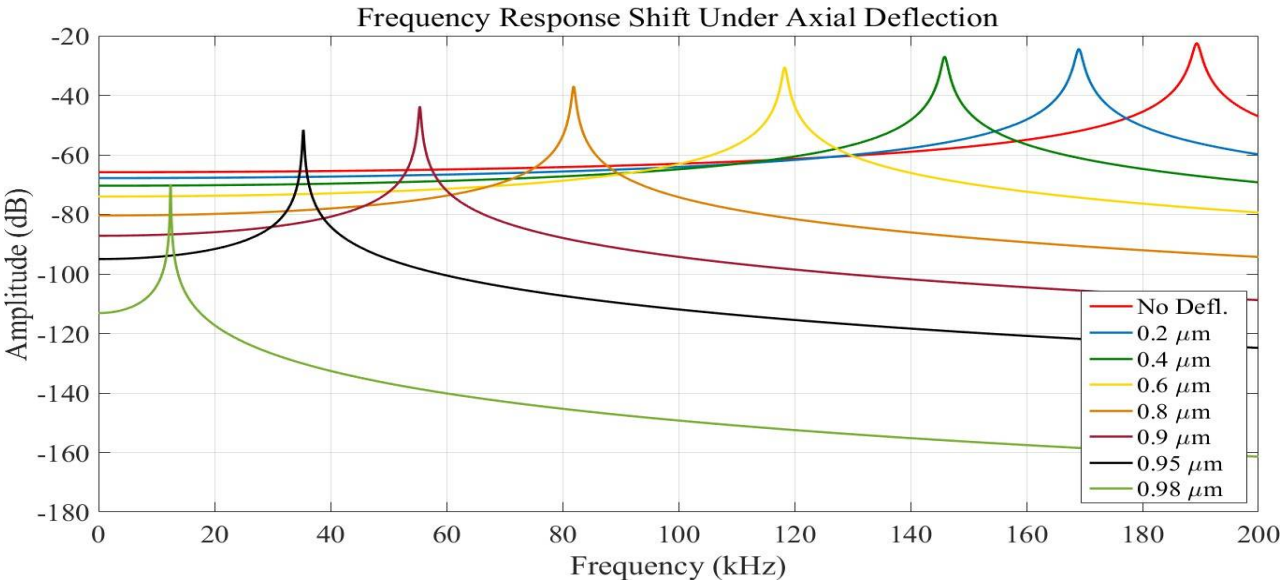

3.2 Energy Loss Mechanisms

For the system, if you want to avoid a large response at the natural frequency of, attenuate the system properly. The damper absorbs an unwanted amount of system kinetic energy and converts it into other forms of energy. A well-known example of this is the suspension of a vehicle. The extra mechanical vibration energy is converted into thermal energy by friction. The less vibration, the more comfortable the vehicle can drive. However, the resonator must vibrate strongly. Therefore for mechanical resonators, reducing the amount of energy consumed by the damper increases sensitivity and signal-to-noise ratio. In addition, the low power consumption reduces the power consumption required for the system. This loss is directly related to the damping ratio of the system. However, the definition commonly used to describe the dissipative behavior of a system is called the quality factor. Here, Q is inversely proportional to c.

As shown in , the following applies: The higher the Q, the better the mechanical and electrical properties of the less dissipative resonator. In this study, the pressure sensor of interest is designed to operate in the air. This is related to energy loss as the air between the structural gaps acts as a damper for the system. When the resonator operates at atmospheric pressure, the loss due to air generally outweighs other inherent losses such as thermal elastic damping (TED), support loss, and surface loss. Therefore, in this design, due to air damping, Q occupies most of the defined whole. F. This section describes an estimate of the quality factor that uses to calculate the optimization. Air damping is extrinsic and can be operated by design. Damping characteristics depend on the activation and capture choice of the parallel plate or side comb fingers. In a design that uses changes in the distance between electrodes to sense changes in the electric field, the elasticity of the air destroys the squeeze film. However, if the electric field detection is due to a change in the overlap length of the electrodes, the air will roll between the plates instead of compressing them. Energy dissipation is due to the viscous force of these laterally moving plates. The latter is called sliding air damping, and this section compares the effects of these two types of air damping because it is important to determine the working principle of capacitive sensing and detection.

Sliding Air Damping

When simulating the flow between two side driven plates, two different types of gliding airflow need to be taken into account. These are referred to as Stokes- and Quet-type flows, respectively. Couette flow, according to Wang, is appropriate for very small gaps in low frequency applications, whereas Stokes flow can be used in high frequency applications [37]. Both are covered by the study's application; however, it is considerably simpler to examine the Quet-type flow. Furthermore, according to a report from [38], comb fingers spaced at intervals of 2 m perfectly adhere to the Quet-type flow assumption. Couette flow is therefore used for modelling. Laminar flow between comb fingers is assumed in this kind of flow. Figure 3.5 displays the side comb fingers' top and side perspectives along with the resistance that goes with them.

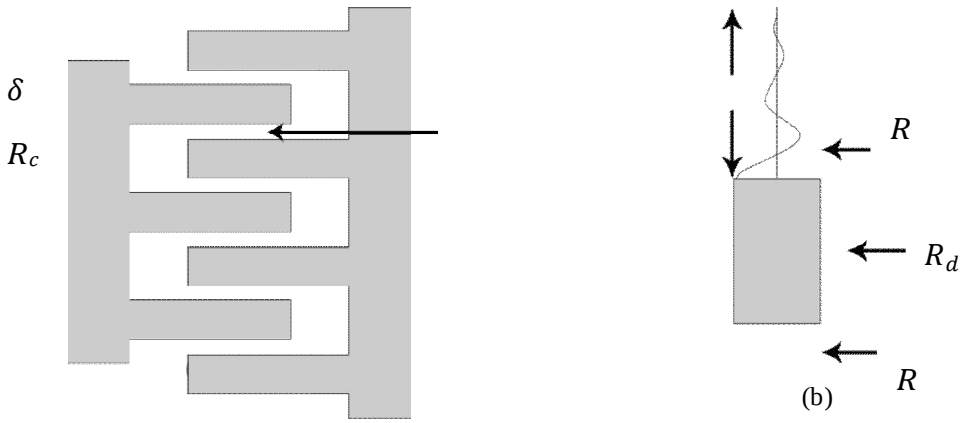

Figure 3.5 - (a) Top and (b) side view of comb fingers with the air resistances shown

Rc represents the drag resulting from slip flow between comb fingers and is connected to the quality factor Qc. Rt, Rd, and Rb are upper, direct, and lower resistances, respectively, and they are connected to the relevant quality characteristics. In Figure 3.5, shows the penetration depth. Beyond this distance, the fluid can be thought of as stationary, according to the definition. This is related to the frequency of the plate and the kinematic viscosity of the liquid [38].

where v is the liquid's kinematic viscosity. would be less that 10 m for just a plate moving at normal temperatures air at frequencies greater than 90 kHz. Since the capacitive plates have now been resolved as well as the liquid at the top and bottom extends more than 10 mm, is taken into consideration when determining Qt and Qb. In fact, these two quality variables are considered the same because they have the same penetration depth. They equal [38] when calculated; Here, μ is the viscosity of air, which is assumed to be 17.9 × 10-6. $Pa{\cdot}s$ and As represent the surface area associated with the decay of the cavity. In this context, this is the total surface area of the vibrating part, including the tine and the capacitive plate. Since the flow between comb fingers is also assumed to be a quet-type flow, Qc is calculated in the same way, This time g is the distance between the fingers, which is 2 μm, and Ac is the sum of the overlapping areas of the comb fingers. Qd However, it cannot be calculated and estimated after testing. Finally, the overall quality factor can be calculated in a consensus format, assuming sliding air dumping.

As other have established, the elasticity of the air between the plates is what dampens the squeeze film. This air is subjected to a continuously oscillating pressure differential via harmonic motion, which results in energy loss. Additionally, there is still slip at the other

resonator boundaries, which contributes to the loss of viscous energy. The Qt and Qb discovered by (2.17), then, remain reliable for identifying parallel plates. You must first compute the air damping coefficient and the spring constant in order to determine the quality factor. The squeeze number is first calculated when using the computation method described in [39].Where P is atmospheric pressure which is equal to $1.01 \times 10^5\ Pa.$ Accordingly, stiffness and damping coefficient is obtained by After calculating the stiffness term $Kair$, you need to add this value to recalculate the natural frequency to get the new effective lateral stiffness of the structure. Next, when the damping coefficient is calculated, the quality coefficient Qp of the parallel plate can be found immediately. Finally, the overall quality factor when using parallel plates can be found by replacing QC with Q .

This chapter shares some of the equations and concepts related to resonant splitting. To process the concept in the same way as the optimization routine, modal shapes are assumed and effective mass and stiffness values are derived. These equations are used to show the decrease in the natural frequency of a simple beam under compressive loads. In addition, a single degree of freedom model is envisioned to estimate the change in frequency response of the same beam when a compressive load is applied. In addition, air damping was studied in two parts: glide air damping and squeeze film damping. The relationship between qualityand estimation of damping factor is disclosed. Finally, this chapter provides some background on the calculations in Chapter 4.

CHAPTER 4

DESIGN OPTIMIZATION

This chapter details design goals and considerations. Describes pressure port design and stress analysis, as well as modal and buckling analysis of resonant structures. The design of this pressure sensor can be divided into two sub-functions. It is a design with a DETF structure that can overcome large displacements such as 100 µm without buckling. Designed a package that can flex the DETF when external hydraulic pressure is applied in the desired deflection range.

4.1 Design of the Package

You need a very simple but effective package. Otherwise, it would be very difficult to manufacture the housing and assemble the structure into the housing. The package design has been kept as simple as possible. The package consists of three main components. These include a hollow internal cylinder into which the measuring element can be inserted, a module with a pressure connection that transfers pressure from the outside to the measuring element, and a seal to seal the hydraulic fluid. Figure 3.1 shows the disassembled and assembled CAD views

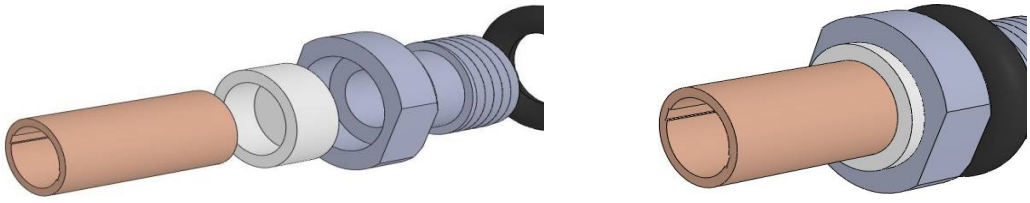

(a) (b)

Figure 4.1 - (a) Exploded and (b) assembly view of pressure port

The main design goal of the package is to withstand water pressure of at least 100 bar while maximizing the deflection of the pressure port diaphragm. However, there are two limitations to the design. First, the maximum stress of the pressure port diaphragm should be less than 138MPa. This value is chosen for aluminum 6061 diaphragms with a yield strength of 276

MPa, resulting in a factor of safety. Therefore, stress and deflection analysis is performed analytically and numerically on the membrane. Second, the diameter of the membrane should not exceed 6.2 mm and this value depends on the maximum diameter of the associated port of the test equipment. Finally, the threads of the pressure fitting connected to the hydraulic circuit must withstand 100 bars. The membrane can be thought of as a circular plate with constrained edges. According to Kirchhoff-Love plate theory, the maximum stress occurs at the edge of the plate. The size of the stress at the fixed edge can be obtained from [40].

where P is the magnitude of uniform pressure in N/m2, r is the radius of the plate, and h is the diaphragm thickness. Maximum deflection under uniform loading occurs at the center point and equals zero to [40],*D* is flexural rigidity in this equation and can be calculated using following,with *v* being Poisson Ratio. When equations are combined and materialproperties of structural steel are inserted, required thickness of the diaphragm can be found.

It is necessary to find the thinnest diaphragm with a diameter of 6.2 mm that can withstand 100 bars. Under these conditions, the maximum achievable deflection satisfying max = 138 MPa is 6.06 m with a diaphragm thickness of 0.72 mm. Under maximum pressure conditions, 138 MPa of compressive stress occurs, satisfying the maximum stress criteria for the design.

The threaded portion of the fastener is another weak point of the pressure port. The thread safety factor under these conditions can be calculated using the procedure outlined below. To calculate the force acting on threads, the thread area is first calculated.

How long is the engagement? D is the major diameter, and p is the pitch size in millimeters. Le, D, and p for the fastener that fits into testing equipment are 4.5, 9.72, and 0.907 mm, respectively. The stiffness of the bolt element and other members of the connection must then be determined. Bolt stiffness can be easily calculated. In order to determine joint stiffness, the stiffness of other members, km, must also be determined. Because the stiffness of the gasket is much less than the stiffness of the other joint elements, the stiffness of the members is assumed to be part of the pressure port is made of steel, which increases the safety factor of the threaded part. In other words, the pressure port consists of two different parts that are locked together.

Aluminum for diaphragms provides higher deflection without yielding, and threaded parts are steel for higher safety factors.

The steel parts of the pressure connection are freely available on the market and can be used in just a few processing steps. This is 9S20 free cutting steel. Substituting the material properties of 9S20 into the above equation gives a factor of safety of 2.89.

4.2 Design of Resonant Structures

A microfabricated DETF element and a package containing the DETF element and its connections to the outer domain make up this design. The DETF is created using microfabrication techniques with sub-m precision, whilst the package is created using traditional manufacturing techniques with a very high degree of precision.Therefore, mechanical springs in DETF elements are made to be able to tolerate at least 100 m of axial deflection without buckling. The major goal here is to safeguard the sensor components. When in contact with the diaphragm, the DETF itself has a tendency to buckle, but a network of spring components that can largely absorb this deflection ensures the DETF's structural integrity. Additionally, when the DETF is installed inside the housing, this helps minimize the impacts of misalignment. Only one end of the DETF has the curved beam-shaped spring member mentioned above. Figure 4.2 depicts an explanation diagram of the designed spring and DETF structure.

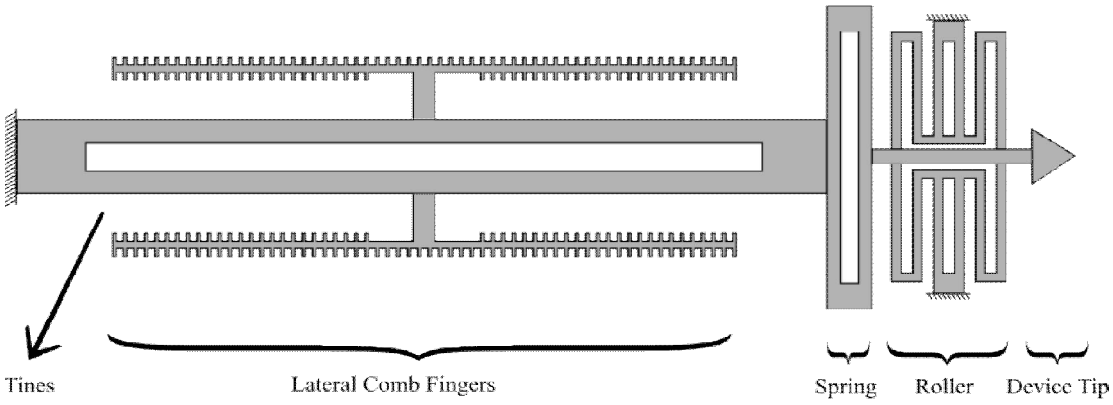

Figure 4.2 - Examples of DETF with lateral comb fingers and its complementary springs androllers

It is also important to eliminate the lateral load, which is dangerous for DETF, as it s easy to damage the tip of the detector. If it is misaligned, the DETF chip may come into contact with the pack and miss the location of the lateral load. Therefore, springs are also used to support the rollers, preventing most of the lateral deflection from reaching the tip of the sensor element.

The usage of lateral comb fingers for capacitive detection is another aspect of the design, as squeeze film damping for parallel plate detection under air operation circumstances is unavoidable. Figure 4.3 displays two different types of capacitances for capacitive plates. Due to fluids flowing between the combs, comb finger type generates air damping. Sliding air damping is preferred over squeeze film damping because it dissipates energy under atmospheric pressure more slowly. Therefore, it is anticipated that the lateral comb fingers will have a higher overall quality factor.

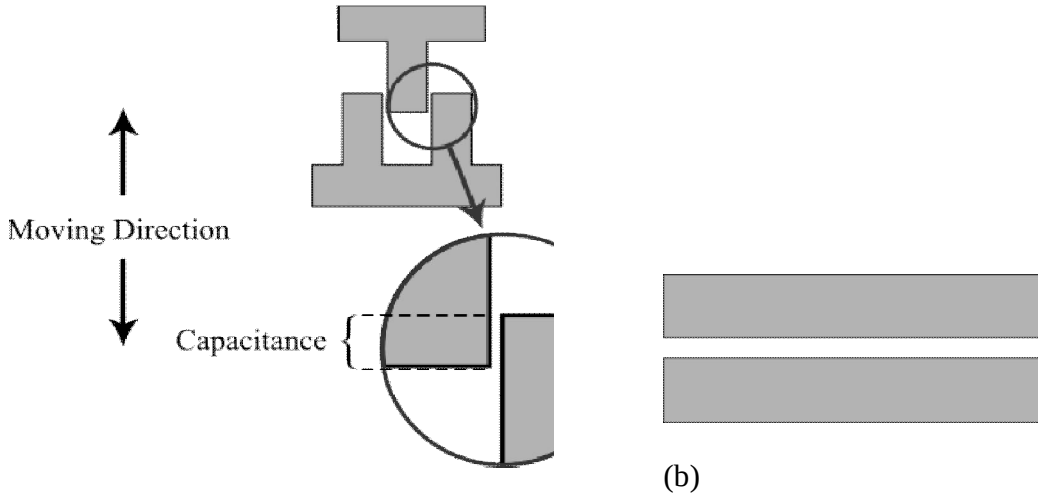

Figure 4.3 - Examples of (a) lateral comb finger and (b) parallel plate configurations

Device dimensions are defined by a optimization algorithm aimed at achieving the highest detection resolution. Various restrictions are set to acquire different devices. Therefore, different dimensions of the device are set for each result. In addition, the design includes simulations to validate the model on which the optimization code is based. In addition, it simulates the effects of axial loads on the tip of the device and provides design criteria that allow 100 µm tip deflection. As a result, all devices have been proven to withstand 100 µm

compression set without buckling. In particular, the Solid Mechanics module in the COMSOL Multiphysics 5.0 package is used for simulation purposes. With this module, you can perform natural frequency analysis using geometry and material properties to find the desired mode shape and the corresponding natural frequency. However, more specifically, we use prestressed natural frequency analysis to obtain the result of axial load and equipment natural frequency.

In parallel with this study mode, steady load cases and frequency analyzes can be calculated. The equations and learning modes covered in this module are known as the Navier-Cauchy equations commonly used to solve linear elasticity problems.

4.3 Design Constraints

Tyne is an important component of the resonant structure, and important properties such as sensitivity, quality factor, minimum detectable pressure, natural frequency, and output voltage are directly related to the shape of the tine. Therefore, optimization of the tine shape is of utmost importance. MATLAB code is generated to improve device performance. The width and length of the tine is optimized by this code. By respecting certain constraints and maximizing the particular mechanical and electrical quality of the sensing element, the code searches for the best values for these parameters within the preset upper and lower bounds. The purpose of the limitation is to design a device that can be properly tested on existing equipment. There are two types of design constraints, these are;Output voltage is greater than 25 mV,Natural frequencies of devices are no greater than 90 kHz.

The objective function of the optimization routine is to find the tine geometry that gives the maximum value to the product of the sensitivity and the quality factor. This feature has been phased out for two main reasons. First, atmospheric operating conditions significantly reduce the quality factor of the device. Second, the spring element that is supposed to protect the device reduces sensitivity by almost a hundredth as a drawback. The quality factor for squeeze film damping is calculated at which requires a high-quality factor and eliminates all parallel plate build devices. Due to the need for lateral comb fingers, the nature of the overlapping capacitance does not change enough to change the gap with lateral movement, so the output voltage becomes an issue. A longer capacitive plate can solve this problem by increasing the number of comb fingers.

Therefore, the operating environment of the atmosphere means that the capacitive plate must be long enough. In this study, the length of the capacitive plate is set to 0.9 times the length of all shapes of Tyne.

4.4 Geometrical Optimization Procedure

It is possible to model the system as a single mass and include the mass of the capacitive plate in (2.5), but the relatively long length of the capacitive plate makes it 90% of the length of the tine. If you are actually dealing with rigid bodies, the optimization will be inaccurate. Against this background, the solutions (2.4) and (2.5) combine all mass elements into one point and omit the operation of the capacitive plate, giving the system a single degree of freedom. To show the effect of this inaccuracy and discuss the acceptability of this approach, a comparison is made between the single-degree-of-freedom model and the results of the finite element analysis under the heading "Results of Optimization". I will. The theoretical background of the calculation by the method is shown on the next page with explanation. These calculations perform half of the DETF modal analysis. Therefore, as shown in Figure 4.4 (a), the desired modal shape is symmetric with respect to the vertical axis, so half of the structure is modeled. The single DOF machine model used is shown in Figure 4.4 (b). $m1$ represents the mass of the upper half of the structure and $k1$ represents the equivalent stiffness of the tine. This is equal to the stiffness of the beam attached to both ends at the midpoint. The damping factor is also included in the model as $c1$. This is the same model as described in Chapter 3.

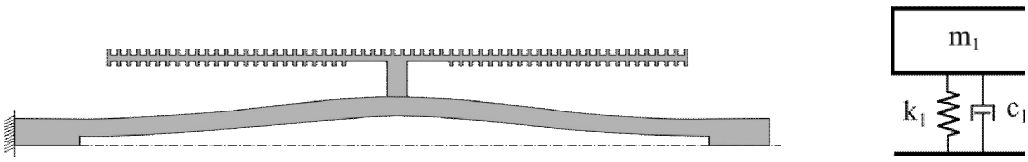

(a) (b)

Figure 4.4 – (a) The DETF component was modelled in the desired mode shape. (b) A single-degree-of-freedom model with a connecting beam, comb branches, and a lumped mass of tine.

While the size of the tines is kept as parameters to the optimization process, the modal analysis is carried out for each possibility that is included within the parameter limitations. This includes natural frequencies in addition towards the relevant mode forms. Next, the output

voltage, sensitivity, and lowest observable pressure are calculated.This code also includes calculations for figuring out the quality factor.

Before getting to the description of the procedures, Figure 4.5 illustrates the structure's dimensions. L stands for length, w for width, and the subscripts p, t, c, and comb, respectively, stand for plate, tine, connector, and comb.

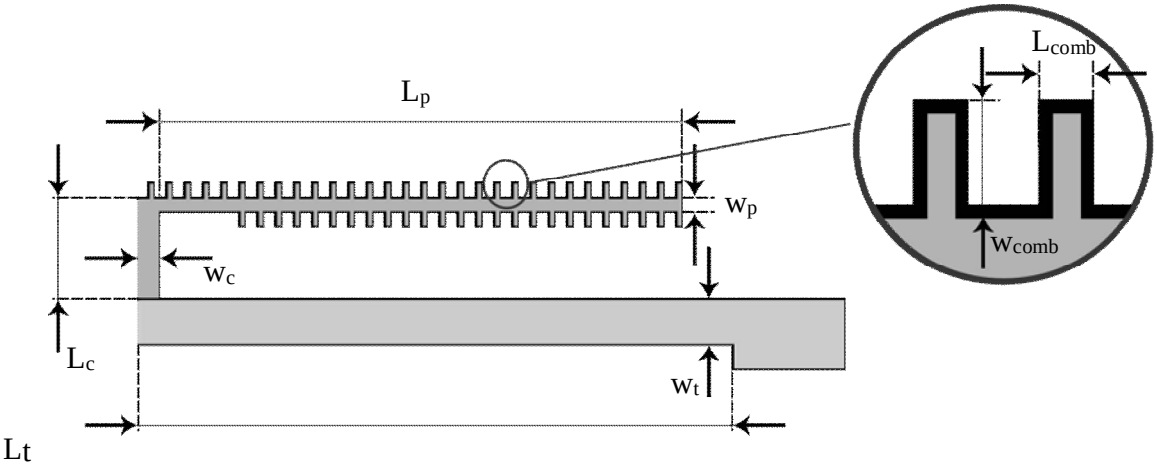

Figure 4.5 - Dimensions of the model

Finding the m1 and k1 values for all viable geometries that fit within the specified range is the first stage in the computation process. It is simple to calculate this step The structure's natural frequency is then calculated using . The fact that only tine is regarded as a flexible body and is harmonically moving in a transverse direction in this mode should be underlined.

Following this phase, all Lt and wt combinations are analyzed and their essential design parameters are identified. The calculation outlined above determines the natural frequency of the selected mode form for all possible geometric configurations.

The sensitivity word shows the rate at which natural frequency varies in response to applied pressure. Thus, unit of this term is simply pressure unit per Hz. It can be calculated numerically as, where P and n denote the pressure and natural frequency, respectively. For a single degree of the model, sensitivity can be numerically evaluated by setting P to a tiny value, such as 10 n bar. Though in a system with only one degree of freedom. Another essential component that has significance for the caliber of test findings is output voltage. Because capacitance changes

0

linearly with respect to tine motion, its computation is somewhat simpler for lateral comb finger arrangement than parallel plate configuration. Therefore, for lateral comb finger structure, non-linear term associated with parallel plate technique is absent. Current output resulting from alternating capacitance should be computed first in order to calculate V out. The capacitance difference between the sensing electrode and the comb fingers of the resonator is discovered .

Resonator motion is translated into voltage in Figure 4.6. The sensing electrode of the resonator is coupled to the trans-impedance amplifier circuit, which converts the current in (b) into an output voltage. As a side note, V t in (b) is 0 due to the fact that proof mass voltage is applied in DC form and does not fluctuate over time. As a result, (b) is simpler.

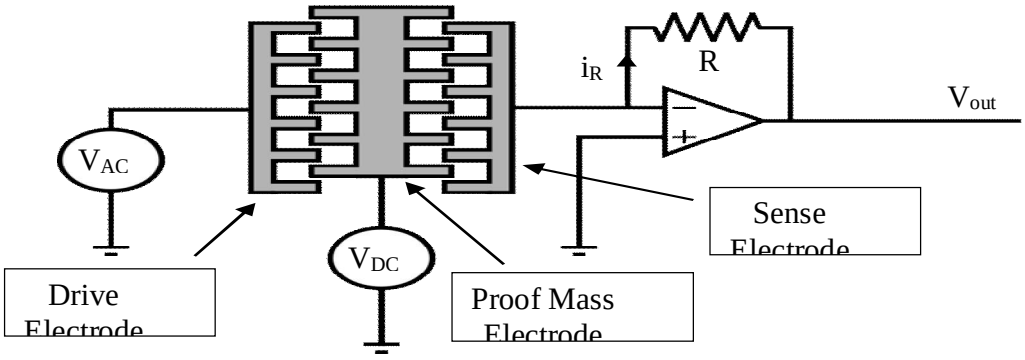

Figure 4.6 - Trans-impedance amplifier shown with resonator

Voltage output for trans-impedance amplifier configuration with $i = i_R$ is Therefore, V_{out} results The smallest detectable pressure is yet another essential sensor property. Additionally, the proposed sensor outperforms the best in the literature in terms of resolution estimate. This sensor's resolution is dependent on the noise, pressure port, and resonator shape. The relationship between the least detectable pressure and amplifier noise is discussed in this section.

It is presumable that noise, specifically V noise, has the worst outcomes possible for V out. The two vectors in this situation should be in a 90o phase, as shown in Figure 4.7. This is the circumstance where V out deviates the most. Due to thermal noise and amplifier noise, V noise is thought to be white noise.

Then V_{noise} can be calculated as explainedby Torrents *et al.* [39];Utilized amplifier which is Texas Instrument's LF-353 has noise properties as follows;

$Input\ Noise\ Current\ (i_n)$: 0.01 $pA/\sqrt{Hz}$

$Input\ Noise\ Voltage\ (e_n)$: 25 $nV/\sqrt{Hz}$

In equation, T refers to temperature of environment in K and k_B is Boltzmann constant being equal to 1.381 × 10^{-23} $J \cdot K^{-1}$. $\sqrt{\Delta f}$ stands for the bandwidth of noise measurementand chosen as 100 Hz for this calculation.

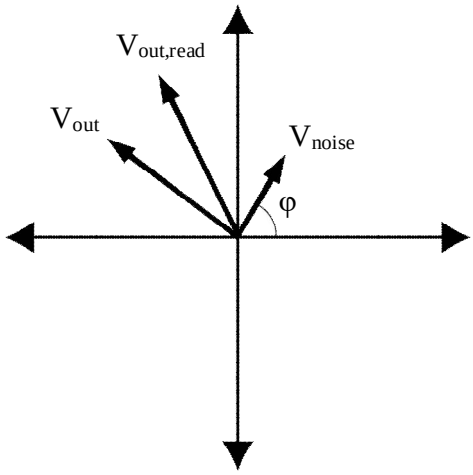

Figure 4.7 – Vectoral illustration of output voltage, voltage noise and read voltage at the worstcase

Then read effective voltage output, $V_{out,d}$ can be written It is seen that, noise with phase φ, deviate V_{out} with a phase of $\Delta\varphi_{noise}$ In addition, quality factor estimates are performed during the optimization process. The theory described in Chapter 3 is used to calculate the quality factor. However, the design includes crash film damping and slip film damping, which are the effects of both air damping. As a result, both are included in the quote. Sliding air damping is done between the capacitive plate and the comb of the electrodes.

This quality factor is calculated using the optimization method according . The damping effect of the squeeze film also occurs between the surface of the electrode and the capacitive plate to which the ridge connects. Despite the fact that this distance (8m) is very long, the loss of squeeze film is a significant loss factor and therefore impairs the quality factor. Quality and are used to estimate quality by squeeze film damping, combining the two qualities.

CHAPTER 5

OPTIMIZATION RESULTS AND NUMERICAL ANALYSIS

5.1 OPTIMIZATION RESULTS

As mentioned earlier, the improvements have resulted in plans to increase the greatest element of quality through device responsiveness. In this way, (3.5) and (5.1) are taken into account when characterizing the elements of the gadget. Table 5.2 shows the results of the rationalization code. Results include assessment of other important electrical and mechanical properties. In addition, some of the internal results are shown in the attached image to explain how the extension code works. The code calculates each property shown in Table 5.1 for the strain selected to characterize the width and length of the tine. Second, avoid ideal print results and results that do not reach normal recurrence values. Finally, select the most ideal aspect of your plan to achieve the maximum value of your aiming ability. The surface view is shown in Figure . The rationalization routine is forced to choose between 500-1200 µm and 10-20 µm for the length and width of the tine. The resistance of the transimpedance speaker is selected to 1MΩ and the proof ground voltage is set to 15VDC. Additional mathematical data is stored in Table 5.1. Constants are taken into account in the rationalization plan.

Table 5.1 - Constants took care of to the streamlining schedule.

Connect or Plate Width	w_c	20 µm
Connect or Plate Length	L_c	120 µm
Capacitive Plate Width	w_p	20 µm
Capacitive Plate Length	L_p	$0.9 \times L_t$
Comb Width	w_{comb}	11 µm
Comb Length	L_{comb}	5 µm
Comb Gap	g	2 µm
Comb Overlap Length	L_{ov}	3 µm

And corresponding results are presented in Table 5.2

Table 5.2 – Resulting design properties of optimization routine and its estimated electrical and mechanical properties.

Properties	Design
Natural Frequency (kHz)	89.99
Tine Width (µm)	16.50
Tine Length (µm)	866.70
Capacitive Plate Length (µm)	780.00
Number of Drive Combs	55
Output Voltage (mV)	25.05
Quality Factor	340

The figure below explains how the cutoff points operate and how the improvement routine chooses the most optimum plan math between as far as is possible. It also shows the midway results. Given that the margins of the surface plot are ventured, the figure below may be confusing. In any event, keep in mind that the diagram's long hub is where these ventured edges are only found. The primary explanation for this is the capacitive plate's length being a design impediment.

These ventured edges might be related to the number of brush fingers, assuming the capacitive plate length is set at 90 percent of the prong length. The brush fingers are spaced apart, so if the capacitive plate's length changes by that much, the brush fingers will either be added to or subtracted from the design. Set this distance specifically to 11 m, then increase the number of search fingers by 1 for every 11 m long. This results in a sudden change in successful mass, resulting in ventured edges on the figure's lengthy hub. Surface plots of the restricting variables voltage result and normal recurrence are shown in Figures 5.1 and 5.2. From these two numbers, it tends to be surmised that the plan is restricted to regular frequencies under 90 kHz.

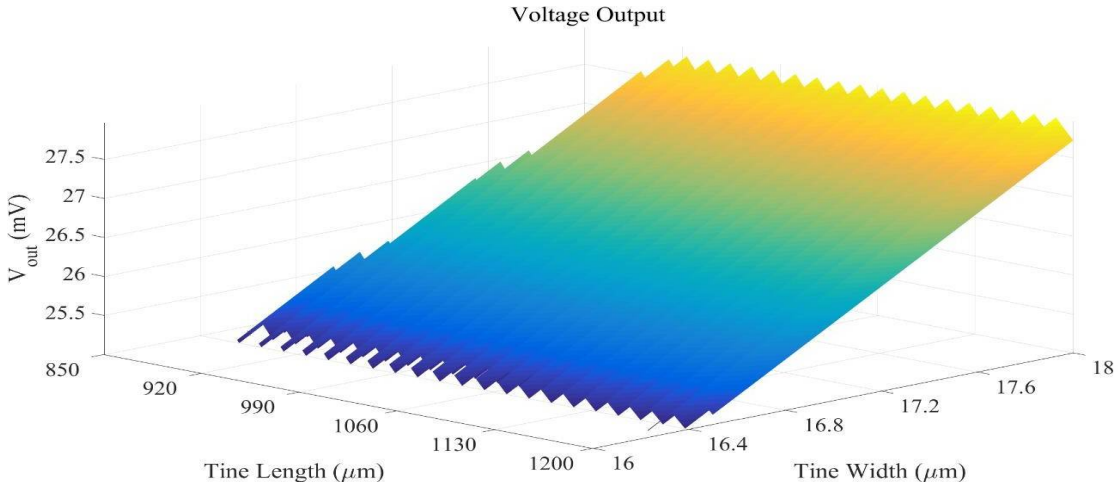

Figure 5.1 - Surface plot of voltage output function which is a limiting factor the design

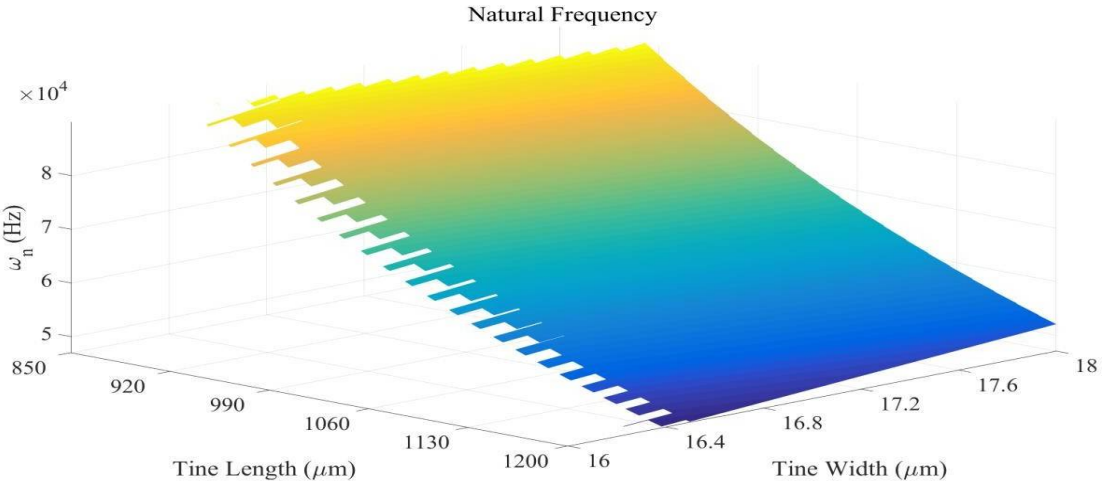

Figure 5.2 - Surface plot of natural frequency function which is a limiting factor the design

The sensitivity and quality factor functions, depicted in the following two figures, are used pick the design. It should be noted that sensitivity is calculated for a DETF that does not have pring and is stated in Hz/m.

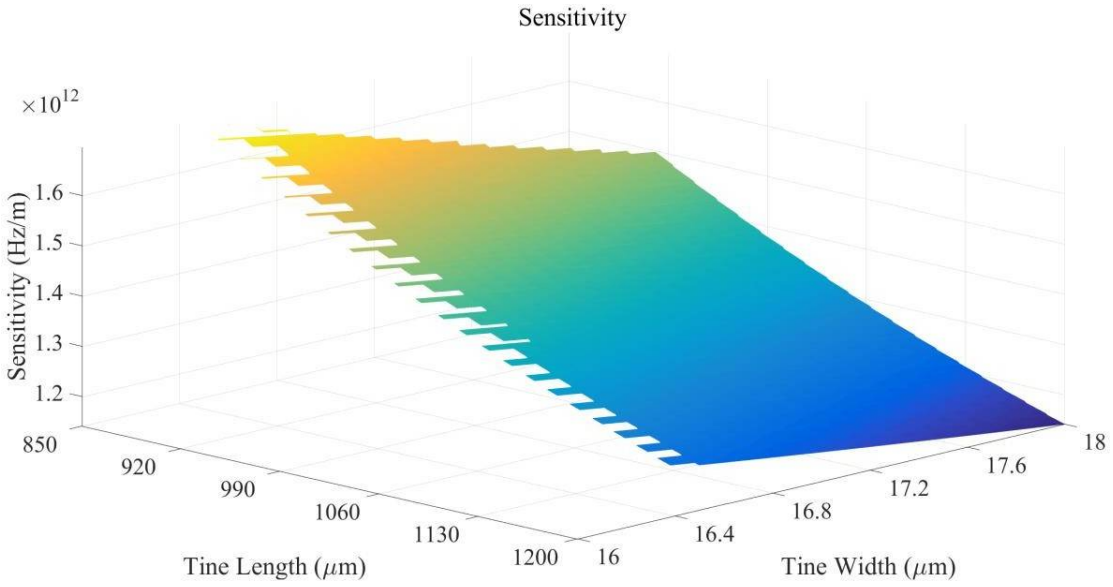

Figure 5.3 - Surface plot of only sensitivity function for all device designs which can satisfy natural frequency and voltage output limits within specified boundaries

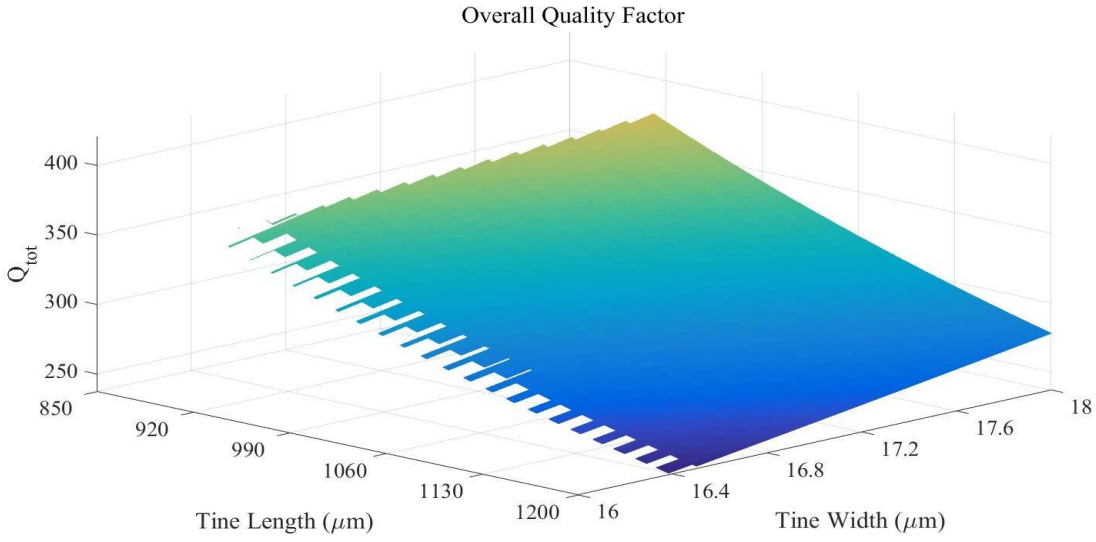

Figure 5.4 - Surface plot of only quality factor function for all device designs which can satisfy natural frequency and voltage output limits within specified boundaries

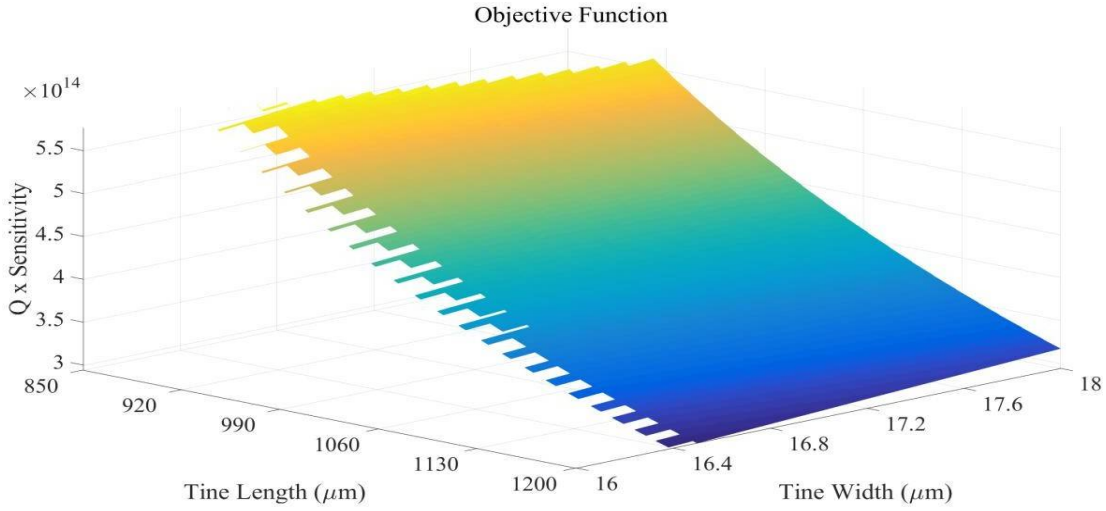

Figure 5.5 - Surface plot of objective function belonging to all device designs which can satisfy natural frequency and voltage output limits within specified boundaries

Finally, the optimization algorithm multiplies the quality factor and sensitivity to get a number whose unit is simply Hz/m, then determines the largest value of this function and outputs the required dimensions. It is possible to read this maximum value and the corresponding dimensions from the top left corner of Figure .

5.2 Numerical Verifications

In this section, a numerical analysis's findings are presented. Using the single degree of freedom model and the COMSOL MEMS Modules, uncompressed resonant frequency was found. Tabular comparisons of these frequencies were obtained. The same instance can also be used to evaluate buckle analysis. Finally, the first eight mode forms of a design are revealed.

Table 5.3 - Natural frequency and percent accuracy of it when found by theoretical model and finite element analysis

SDOFModel		COMSOL
89.99 kHz	14.0%	78.95 kHz

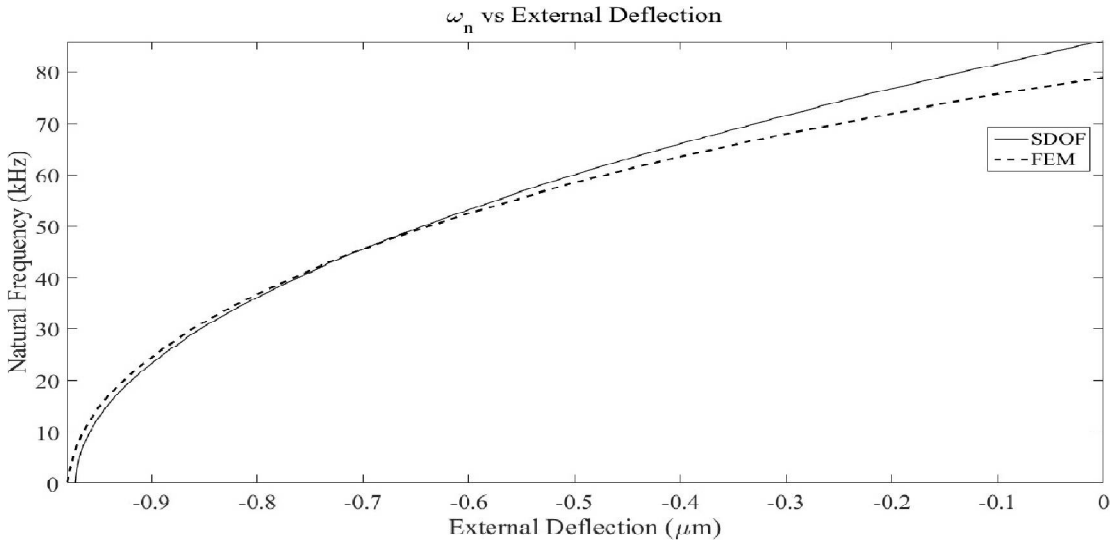

Figure 5.6 - Comparison of numerical and theoretical solutions on axial loading vs natural frequency graph for Design 1

Capacitive plates are designed to have a length that is 90% of the length of the prongs, which is a value that may lead to non-linearity. As a result of the model's assumption that capacitive plates will be firm, there was confusion foreseen between the single level of opportunity model and the reproduction results. However, Figure 5.6 demonstrates that the hypothetical model deviates most from the reproduction data at the zero-avoidance position. Model combination and precision increase as the stacking process progresses. Therefore, one may claim that the single level of opportunity paradigm makes sense for this streamlining.

The length of the capacitive plates, which is specified to be 90% of the length of the prongs, is a factor that could lead to non-linearity. Given that the single level of opportunity model takes unbending capacitive plates into account, a discrepancy between model predictions and actual finds was thus expected. Despite this, Figure 5.6 demonstrates that the zero-diversion point is where the information from the hypothetical model and reenactment differs the greatest. The model combination and exactness increase as stacking progresses. Therefore, it may be said that this streamlining is appropriate for the one level of opportunity paradigm.

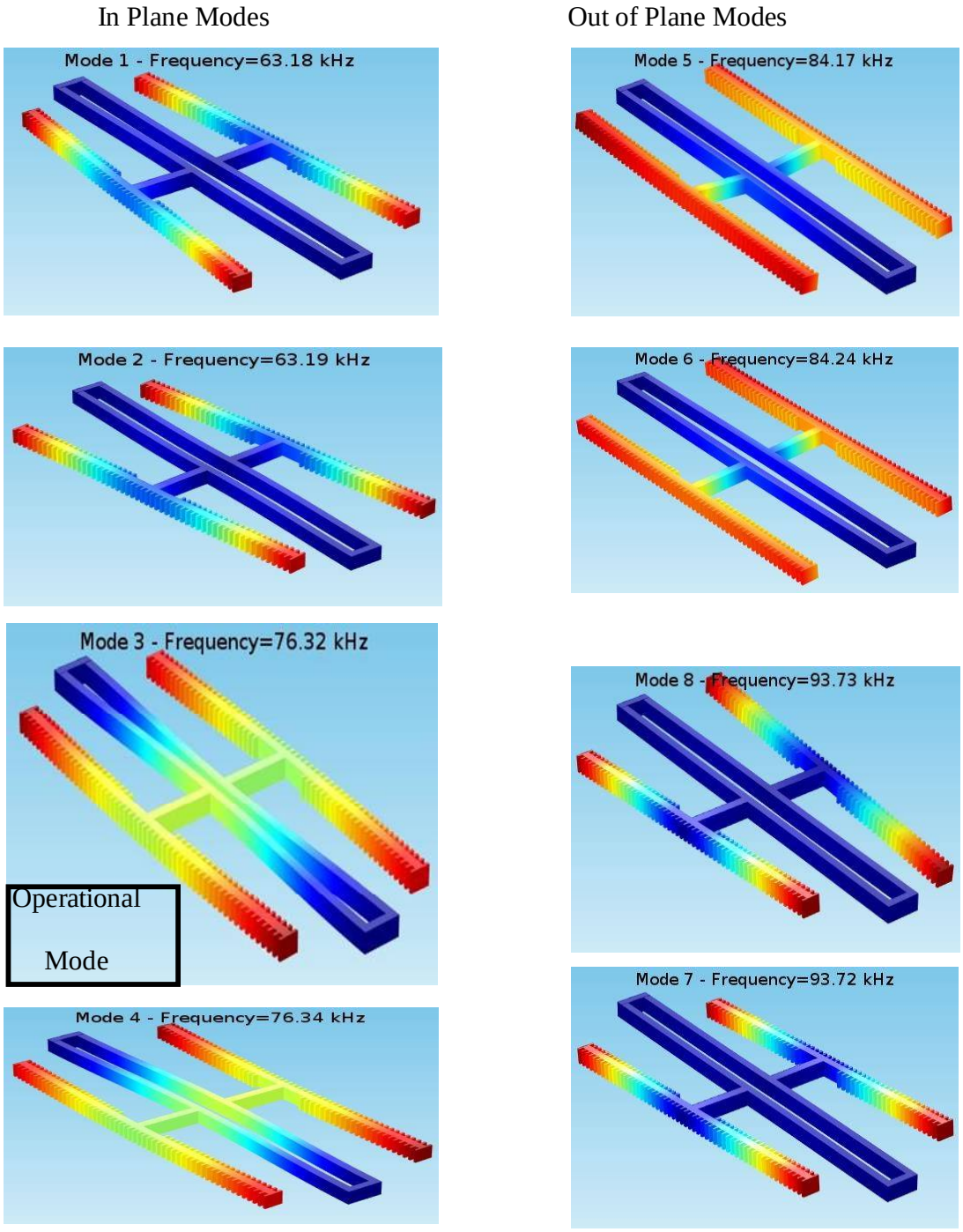

Figure 5.7 - The first 8 mode shapes of DETF with corresponding natural frequencies and order. In plane and out of plane modes are well separated and they are shown in separate columns

5.3 Design of Supplementary Structures

A spring and a roller element were included at the start of Section while discussing the design's concepts. Figure depicts an exemplary view of these extra elements, as well as their junction positions with each other and the tuning fork. The intention behind these additions was previously mentioned in terms of safeguarding the device. Since buckling for DETF alone occurs at 1 m, as can be shown from Figure 5.6, the spring must absorb 100 m of deflection while only transferring around 1 m to DETF. Actually, the goal of including a spring in the design is to increase the x axis of the curve in this illustration by 100 m. In order to counteract the impact of, a roller element is included.

The basic issue with these pieces is that taking care of a deviation of 100 m is extremely troublesome. It is concluded that demonstrating the effect of such redirection is expected for indicating spring math. Diversion and stress examinations are done utilizing the COMSOL Multiphysics MEMS Module, and the elements of the parts in Figure are found. The way that both of these parts can avoid by 100 micrometers and that stacking can influence both the spring and the roller simultaneously in recreations is one more motivation to involve them for examination. Since reproductions were adequate and basic enough for this part of the plan, scientific methodologies were not thought of.

Since it can likewise influence yield, a fruitful plan of gadget parts is significant for microfabrication. Thus, it is chosen to utilize a spring comprised of two major collapsed radiates fit for accepting 100 m of diversion as the accessible space for one sensor advanced. Just pivotal burdens can arrive at the roller component since it is connected to the spring development. It comprises of four collapsed radiates that are held up in the middle by four extra one-sidedly secured radiates. The yield strength of silicon, which is around 7 GPa [1], fills in as a limitation for the meaning of this spring component. Notwithstanding, to be protected, the greatest pressure is restricted to 1 GPa.

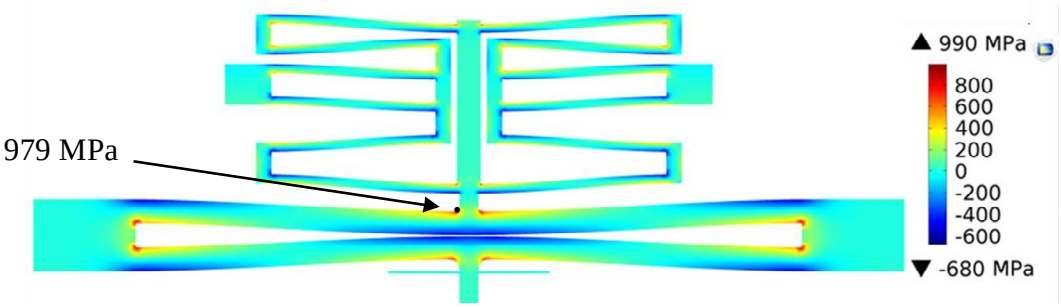

Figure 5.8- Deformation of supplementary elements under 103.5 µm of axial tip displacement.Point of maximum compressive stress is shown. DETF in the model is not shown for salience.

Reenactments uncover that the gadget's local recurrence was marginally moved to 79.48 kHz with the expansion of the roller and spring to the development. Since the assistant designs are not moving at the predefined mode shape, there ought to hypothetically be no distinction. Be that as it may, by and by, prongs truly apply symphonious driving to the spring component, which slows down the ideal mode also. To that end a slight change is expected.

The site of greatest compressive pressure and its relating esteem are displayed in Figure 5.8, which is a screen catch from a FEM bundle. As would be normal, the convergence of the roller's pillars, where the corner's filet has the most limited range, is where the biggest emphasize point is found. Figure likewise incorporates a dimensioned delineation of the relating calculation .By fragmenting the plan into three sections, the point-by-point plan of the sensor is shown. The plan of the bundle is depicted in the initial segment alongside the fundamental wellbeing estimations. These incorporate the calculation of clasp and stomach wellbeing factors. The subsequent piece goes over resonator structure advancement. Specifically, calculations of mechanical and electrical properties are shown, along with meanings of goal capability, plan boundaries, plan limitations, and suspicions. These attributes incorporate the sensor's goal, awareness, voltage result, and reverberation recurrence. Also, mathematical outcomes are utilized to affirm the aftereffects of the enhancement code. The plans of supplemental designs are furnished in the last part along with their objectives and mathematical

CHAPTER 6

FABRICATION

The manufacturing of the suggested sensor is described in this chapter. The manufacturing process consists of two steps: the surface microfabrication of a MEMS sensory component, which requires a number of cleanroom procedures, and the production of a pressure port, which can be produced using only a few elementary conventional machining techniques. This section starts out by describing the traditional machining process used in the machine shop of the mechanical engineering department at METU to create a pressure port. Second, the primary methods of surface micromachining are shown.

*6.*1 Manufacturing of Pressure Port

A hydraulic test rig must be compatible with the design's first restraint for the pressure port. As a result, the Bosch Rexroth Hydraulic pressure setup, which is accessible at the METU Mechanical Engineering Department Automotive Laboratory, is examined, and the appropriate pressure port geometry is established. The pressure port is made of two distinct materials. Steel is used for its superior strength at the threaded section, while aluminum is employed because it has excellent yielding qualities in the diaphragm part.

With an exactness of 0.1 mm, both of these parts are delivered on a customary turning machine. Then, at that point, an obstruction fit is utilized to join these parts to each other. With 100 m of obstruction and two pieces cinched together, the impedance fit is created.

A metal chamber is joined to the strain port as an extra part to permit the sensor board to slip inside. This part was fitted into the construction, however this time it was a free fit so it very well may be changed from now on. Figure 6.1 presentations the tension port that was at last gotten. Notwithstanding the plan's proposal of 0.72 mm for a security element of 2, the strain port really utilized has a stomach thickness of 1 mm because of assembling capacities.

This further diminishes responsiveness, yet it is OK to do as such to show the thought.

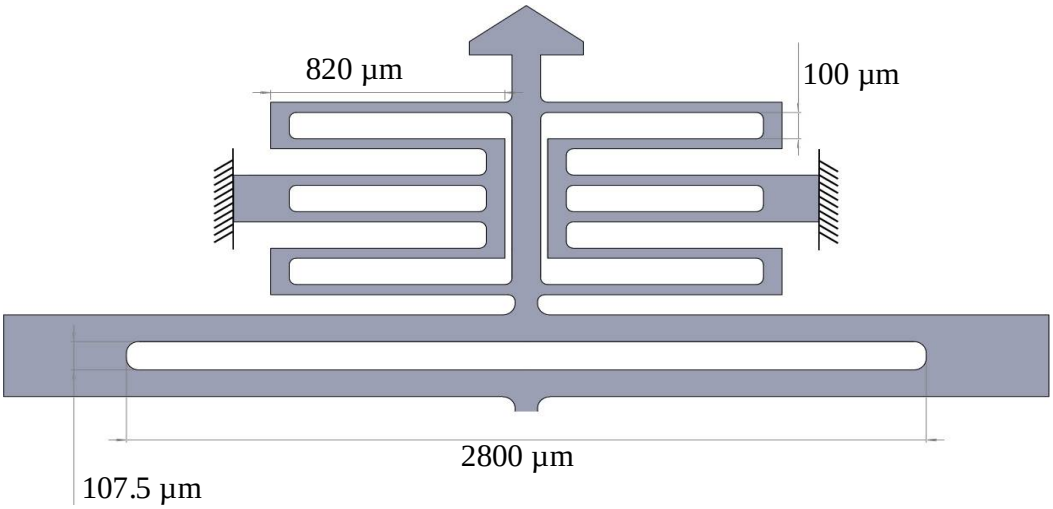

Figure 6.1 - Picture of a manufactured pressure port

6.2 Fabrication of MEMS Sensor

To have predominant gadget properties while keeping up with the gadget layer's protection and requiring only 3 veils, the creation stream displayed in Figure 6.3 starts with a wafer of type 100 SOI. The gadget layer thickness on the SOI wafer utilized in this creation is 35 m, and the handle layer thickness is 350 m. The covered oxide layer is 2 m thick. Piranha draw is utilized to eliminate any extras from assembling methods like compound metal cleaning, despite the fact that it starts with a pristine wafer. Covering 0.7 m of Cr/Au as a metal layer in falter with thicknesses of 30 and 300 nm, separately, is the second stage simultaneously. Covering 0.7 m of Cr/Au as a metal layer in falter with thicknesses of 30 and 300 nm, separately, is the second stage simultaneously. The subsequent stage is to shape the metal layer utilizing a wet engraving to make interfacing cushions for the design's terminals. Gadget layer is carved in DRIE after metal designing.

Gadget layer is 35 µm and this layer is minimal over carved. Then, at that point, in the fifth step, it is expected to draw the handle layer in a similar way to be capable delivery the vibratory pieces of the design. As a cover to deal with layer carve, 0.5 µm of PECVD oxide is covered on the posterior. Nonetheless, emerging issue with handle layer carve is, in the wake of utilizing DRIE on one side it is challenging to apply designing on the contrary side on

account of the pipes which are opened on this surface. These pipes forestall vacuum holder of spinner and aligner gear from holding the wafer appropriately. Thusly a fake glass wafer is utilized for restricting the wafers together for lithography. Photoresist of a similar kind is utilized for restricting. In the wake of restricting, glass wafer is vacuumed by spinner and handle layer is turn covered cautiously and posterior example is applied. Then, at that point, RIE of rear oxide veil happens, a short time later handle layer is scratched with DRIE.

At long last following the last DRIE process, creation continues with the sixth step which is DRIE. In this step covered layer of oxide is stripped involving silicon as veiling layer. In any case, rather than this BHF arrangement can likewise be applied to deliver the designs.
Because of the way that deduction of gadgets doesn't need dicing, after this last microfabrication step, the gadgets are promptly accessible for utilization. Gadgets are appended to branches that are safeguarded during the cycle during the plan stage. Figure 6.2 portrays one delineation of these branches on the cover that is utilized for the handle layer scratch. Noticing that this is a dull field veil and that positive photoresist is being utilized for covering, it ought to be noticed that these gadgets are effectively fragile from the branches like natural product. Moreover, branches are recessed at favored regions for accommodation and consistency. These spaces start the break as it breaks and stop improper break engendering.

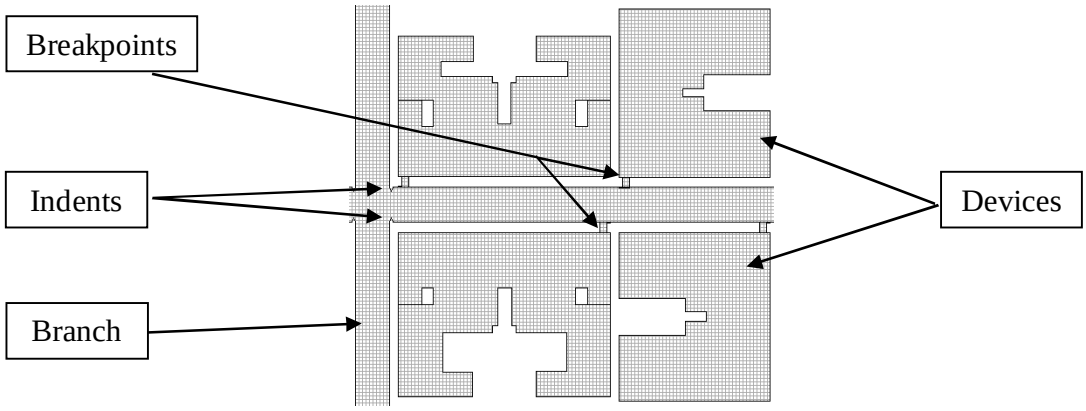

.

Figure 6.2 - Example of a layout drawing view of one of the branches to which devices areconnected.

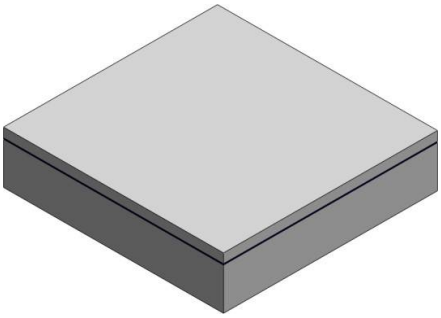

1 - SOI Wafer

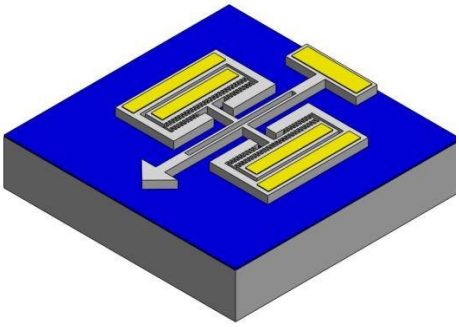

4 - Device Layer Etch (Deep Reactive Ion Etching)

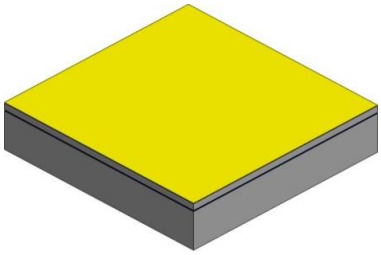

2 - Metal Coat (Sputter)

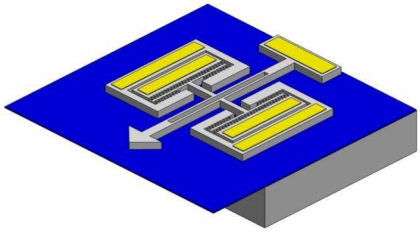

5 - Handle Layer Etch (Deep Reactive Ion Etching)

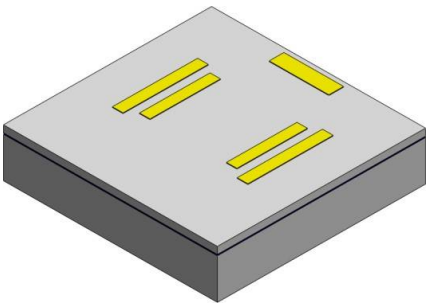

3 - Metal Layer Etch (Wet Etch)

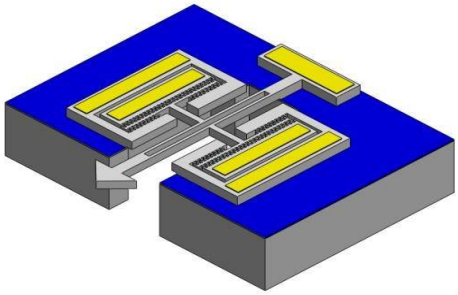

6 - Buried Oxide Layer Etch(Reactive Ion Etching)

Figure 6.3 3D illustration fabrication process steps of resonator. Blue and yellow colors represent oxide and gold, respectively while the grey layers single crystal silicon.

Because fabrication is a very sophisticated process, standardizing and enhancing it really is difficult. Although there have been few attempts to do so in this study, it is possible to go over each step in great detail and optimize the manufacturing for the best output. More study may be done to standardize the approach; however, the manufacturing procedures are only glanced over here and no additional information is offered.

Images of devices acquired with a scanning electron microscope are shown in Figure 6.4. These illustrations are meant to represent the tuning fork resonator as well as the spring and roller components. The first image is a close-up of DETF for this purpose, while the second image captures all three components of a devices.

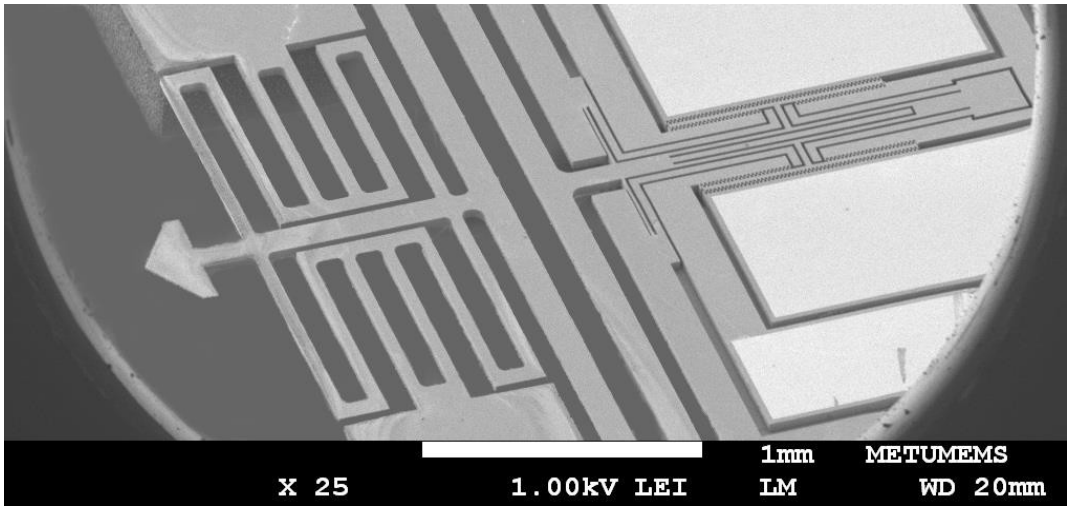

Figure 6.4 - Wide view of tip, roller, spring and tuning fork with SEM

The manufacturing of the sensors is described in detail. The first pressure port element production process is disclosed. This component is produced using a standard turning machine. Second, the cleanroom techniques and related design issues are discussed. Three-dimensional illustrations of microfabrication procedures are provided to aid the presentation of operations. Finally, images of the resulting devices taken with such a scanning electron microscope are exhibited.

CHAPTER 7

CHARACTERIZATION

Following manufacturing, each device is individually examined for resonant qualities. The characterization technique and associated findings are given in this section. The construction of the device is also detailed in the context before the hydraulic pressure test.

Tests can be discussed in mainly 3 different categories. These are;

1. Resonance test
2. Displacement test
3. Hydraulic pressure test

The first step's goal is to assess whether or not the subject gadget is functioning properly. After that, displacement tests were performed to evaluate the device's performance under axial loading. The device's sensitivity is computed based on the results of the displacement test, and the device's reaction is studied. The sensory body is instead assembled in the last stage of testing, and the device is tested in real-world conditions.

As mentioned in the presenting section, digitizing a resistor's output is much simpler. The only components of the location conspiracies shown in Fig 7.1 are a power supply, a network analyzer, and a trans-impedance speaker. Give DC voltage to the verified mass is the objective of the power supply. This voltage creates the capacitance between the sensing terminals and the resonating mass. The construction is driven to reverberate using a network analyzer. The network analyzer assessment and evaluation the AC drive voltage to drive the terminals in a certain repetition stretch while also gathering the yield voltage. The resonator then exhibits a repeating response.

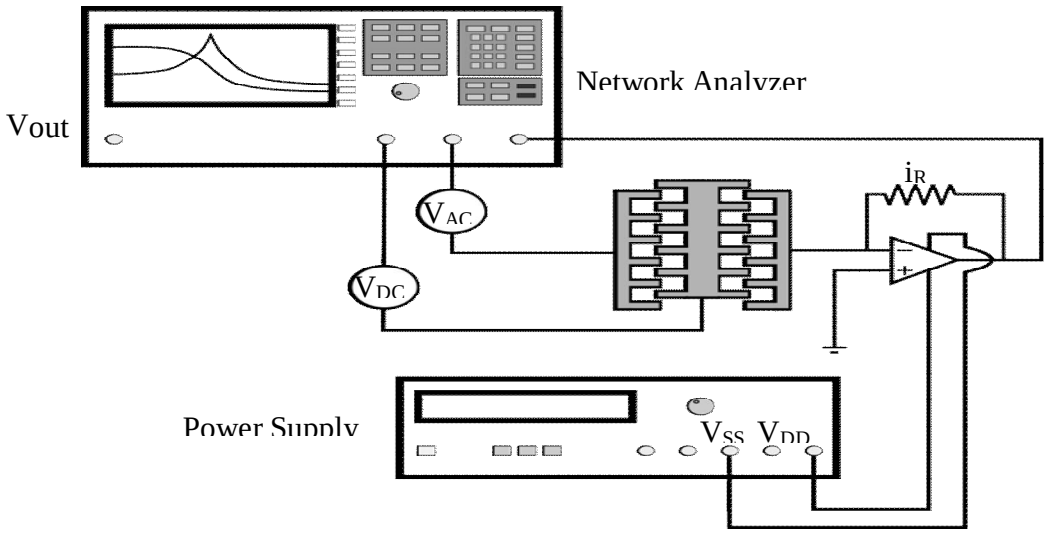

Figure 7.1 - Schematic drawing of detection setup consisting of a network analyzer, DC powersupply, resonator and trans-impedance amplifier.

Instead of current output voltage is preferred form of output because it is easier to handle.It can be fed into network analyzer which compares drive and sense signals directly to obtain frequency response. Essential reason for presence of trans-impedance amplifier is the need for converting current into voltage. Output current rises from alternating capacitance between sense electrode and proof mass. This current is then converted into voltage with help of an operational amplifier and a resistance named as gain. The conversion is discussed later in design chapter while computing output voltage.The above shown discovery strategy is one of the most straightforward approaches to identifying regular recurrence of a resonator. Be that as it may, in this strategy the regular recurrence is found by checking a recurrence span. For the proposed sensor, it is recommended that utilization of tension changes regular recurrence. Consequently, at each unique strain esteem, filtering happens which clearly is exorbitant concerning time. Subsequently further developed strategies comprising of electrical circuits are carried out, for example, self-reverberation and stage lock circle. These are unrivaled shut circle normal recurrence discovery techniques used to drive the resonator at reverberation generally. In any case, this kind of estimation is likewise enough for this review since it is unimaginable to expect to distinguish the tension of pressure driven liquid inside electronically because of states of arrangement. Notwithstanding, it very well may be a decent legitimacy on the off chance that the goal of the sensor was estimated. Consequently, utilizing these shut

circle reverberation circuits and estimating least perceivable tension is left as a future work.

7.1 Resonance Tests

This initial test is performed on all dies using the equipment provided in Figure 7.2 and the circuit described in Figure . Furthermore, Figure 7.1 shows the setup's overall layout. During resonance testing, sensors were not installed on a package surface, and electrical connections were not disconnected. Consequently, connectivity between the MEMS electrodes and the setup is achieved utilizing a probe station.

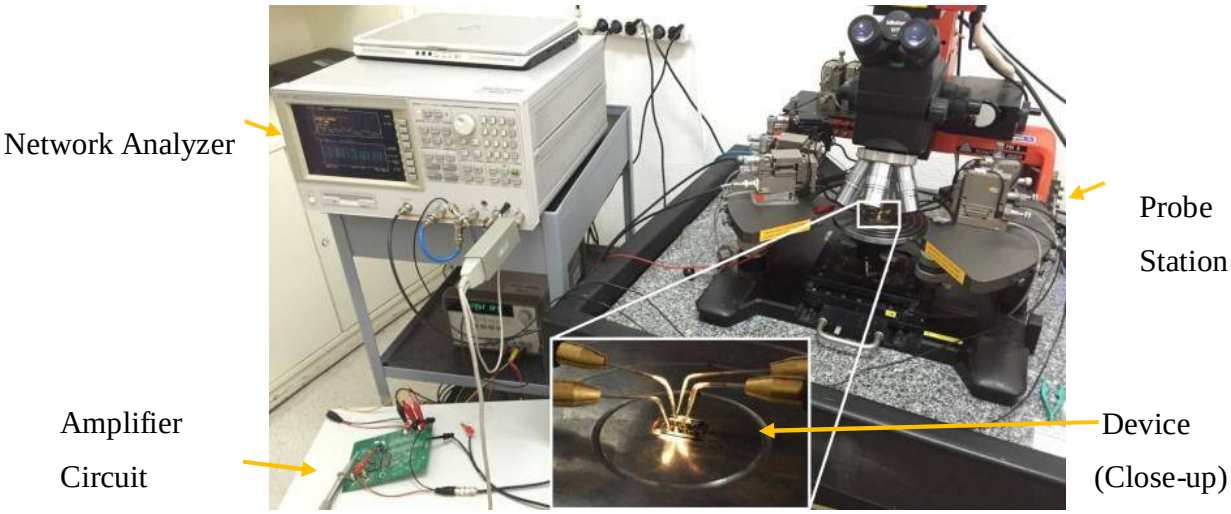

Figure 7.2 - Picture of test setup, network analyzer, power supply, probe station and sensor.

The network analyzer configuration must be supplied for coherence. First and foremost, the equipment is an Agilent 4395A Network Analyzer. An AC signal with a power of 15 dBm watts is used to drive sensors to resonance. Using a network analyzer, a 40 V DC voltage is delivered to that same proof mass. The bandwidth for measurements is set to 30 Hz, and sweeps are performed at 801 points. It is important to have a bigger frequency interval than IF bandwidth between each data point.

Quality factor scores of up to 260 have been observed in such tests. This is related to atmospheric operation circumstances, although the low-quality component has a significant impact on the outcomes. Nonetheless, Figures 5.3 and 5.4 show two of a related outcomes. The first figure depicts the frequency response of a proportionally operated sensor. This implies that

it is powered by two drive motors and detected by two sense electrodes. The second illustration represents a sensor with one motor and one sense electrode, resulting in asymmetrical functioning. As a result, more than one peak in the frequency response is predicted. The latter is likely caused as such by a dust particle that inadvertently linked two electrodes. The latter is likely generated as such by a dust particle that inadvertently linked two electrodes and deactivated those electrodes. The non-enclosed sensor design is mainly accountable again for dust vulnerability.

Figure 7.3 - Frequency response of a sensor which has a quality factor of 158. Note that jump inthe phase curve is due to reaching -180 degrees

In the second result, 2 fused peaks are observed which is mainly due to aforementioned asymmetric drive conditions. And even there is a small peak on the left around 72 kHz.

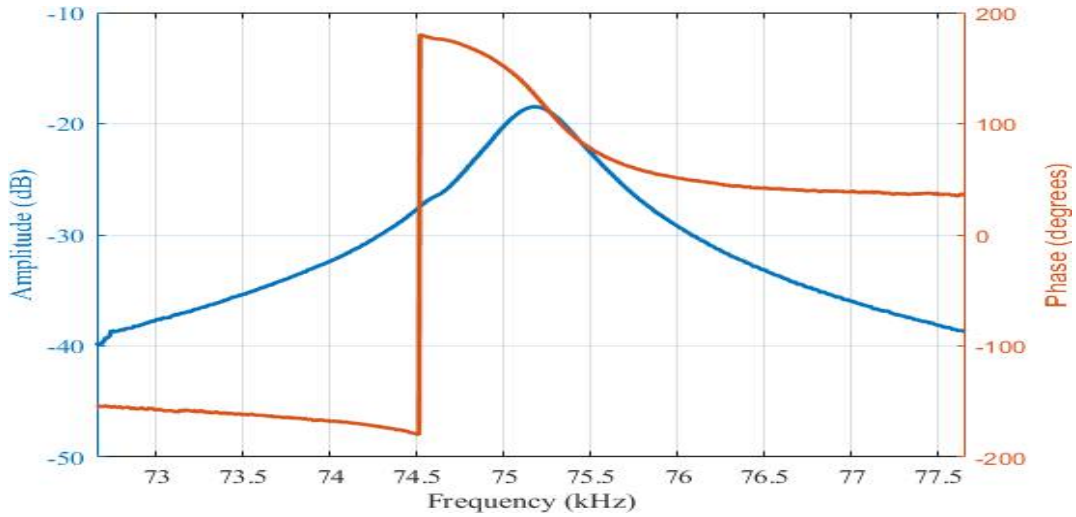

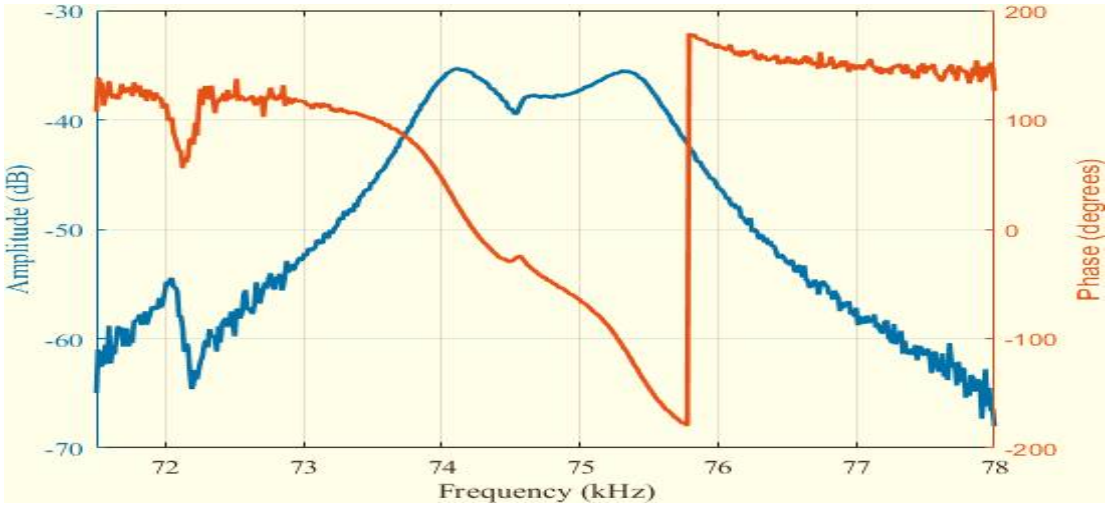

Figure 7.4 - Frequency response of a sensor driven by only 1 electrode asymmetrically. Q valuesrelated with peaks are 134 and 75, respectively.

7.2 Displacement Tests

One of the sensors is subjected to displacement testing. Sensors are vacuum-fixed to the surface of the probe station table, and a metal portion is attached to the rear of the sensors to ensure that it is securely fastened. Figure 7.5 shows this setup. Also visible in this image is a piezoelectric actuator with a metal portion put on it to aim the device's tip.

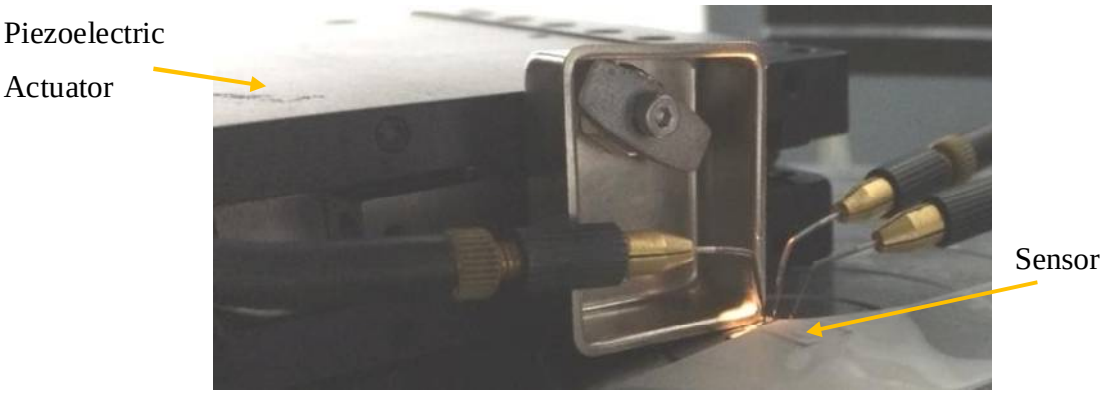

Figure 7.5 - Additional equipment for displacement test setup and fixing of the sensor. Sensor tip is deflected with piezoelectric actuator's upper half with the help of additional metal parts.

The lowest progressive linear motion of such piezoelectric actuator with the power source employed is roughly 3.3 nm/mV, which is enough for testing. Measurements are performed every 1 V change for the 25 V range and every 2 V for the 50 V range, which amounts to 6.6 m of deflection. The results of 25 V and 50 V scale testing are shown in figures below. It should be emphasized that testing do not begin at zero deflection; rather, the actuator is put extremely close to the tip under the microscope with no contact. When a frequency change is seen with increased actuation voltage, the test begins. The starting voltage for the first result is discovered experimentally to be 11 V, however this is not precisely known. In contrast, on the second test. In contrast, the beginning value for the second test is anticipated to be roughly 12.86 V. Interpolation is used to approximate this value. The number are analyzed by measuring the amounts for resonant frequency produced by the first and second rising steps of voltage.

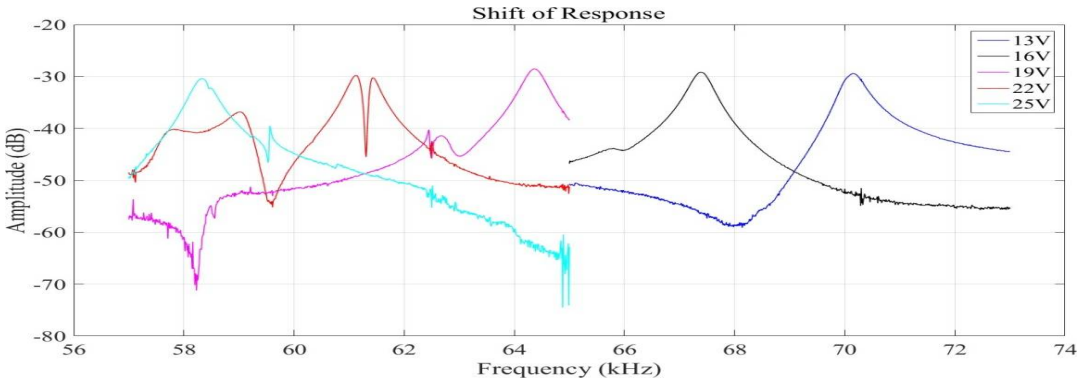

Figure 7.6 - Resulting responses from the first loading with a scale of 25 V actuation voltage.Note that shift started at around 11 V.

Figure 7.6 depicts device response under various loading scenarios. The tested voltage range was 25 V. Following this test, it is discovered that the scale may be raised. Figure 7.7 shows the result of the larger size test.

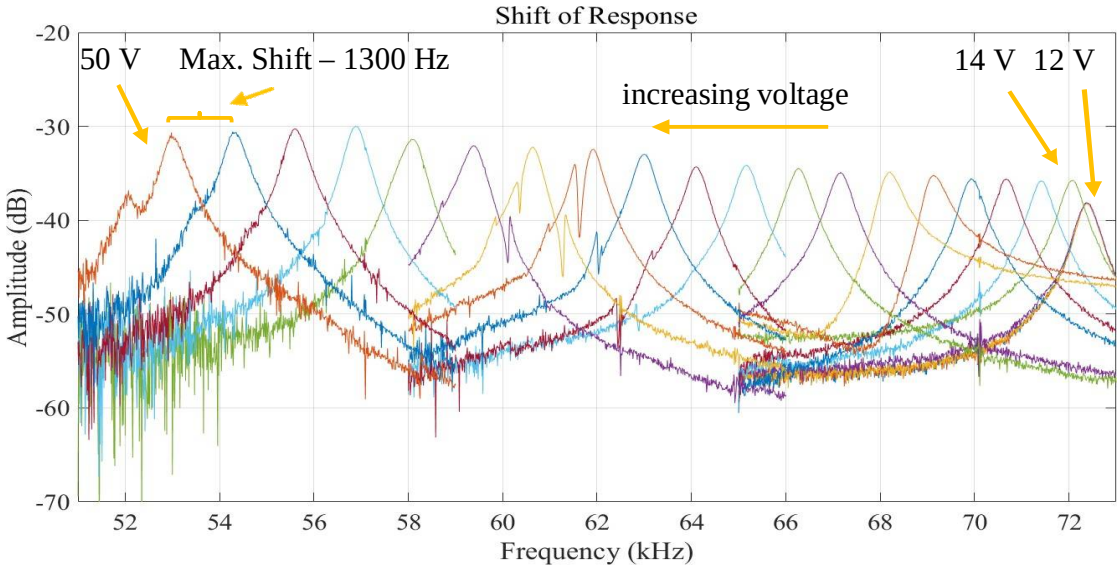

Figure 7.7 - Frequency response curves when the voltage is increased to 50 V. Note that stepincrease in piezoelectric actuation voltage is 2 V

The maximum shift occurs at the end of the scale and is 0.65 kHz/V, while the minimum change is detected between 14 and 16 V and is 0.34 kHz/V. This exam is done in reverse sequence without a break. Figure 7.8 depicts the corresponding findings.

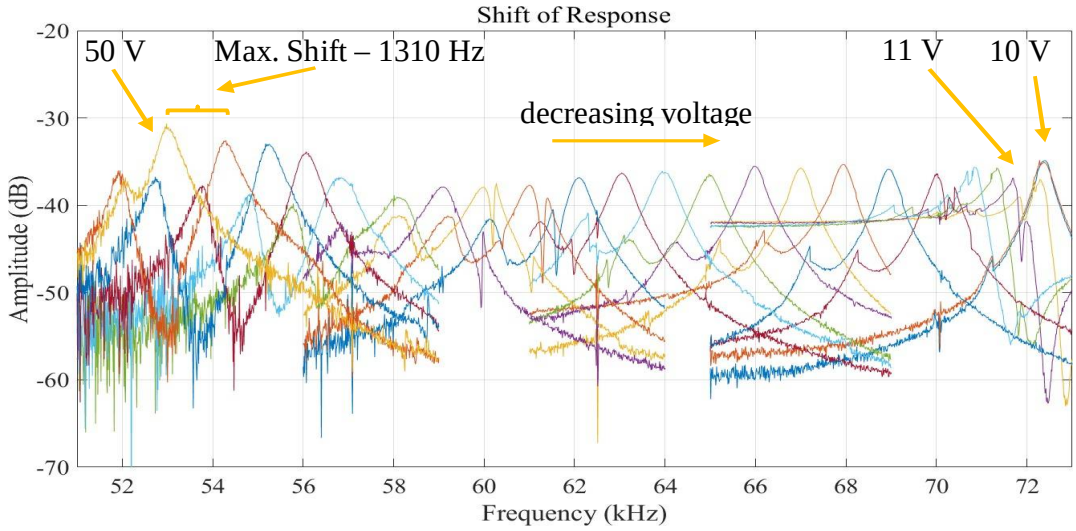

Figure 7.8 - Frequency response curves when the voltage is decreased from 50 V. Note that step increase in piezoelectric actuation voltage is 2 V

During unloading testing, the actuating voltage is lowered from 50 V to 2 V till the tip is liberated. It can be noticed that this time tip restored to its initial state at 10 and 11 volts. The result of interpolation is a release voltage of 10.31 V. However, the projected starting voltage was 12.86 V. This was to be expected since, even if the setup is as excellent as it gets, position changes are unavoidable.

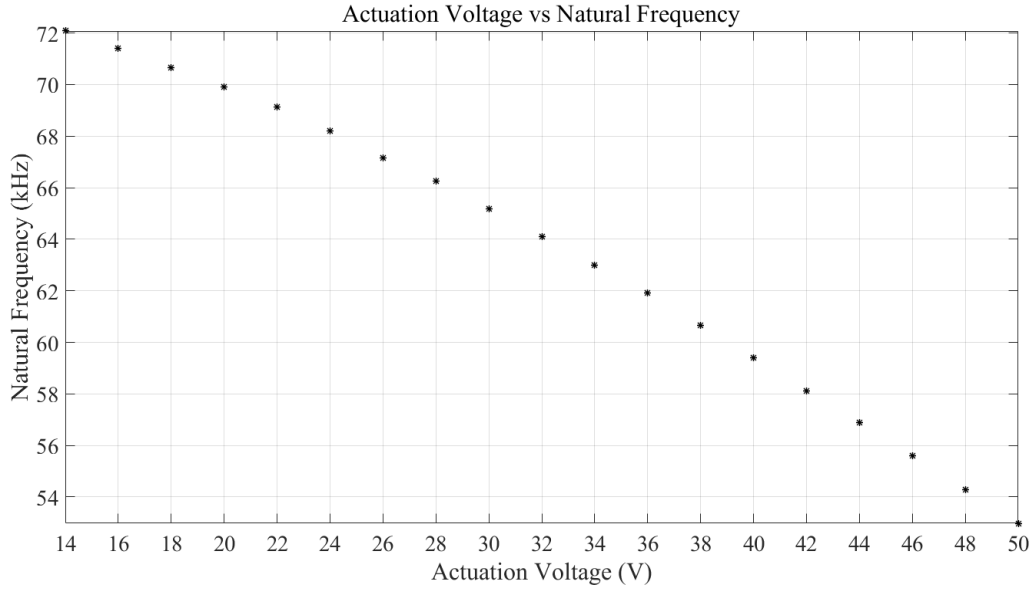

Figure 7.9 - Graphical illustration of the results of the second displacement test

Figure 7.9 depicts the frequency response derived from Figure 5.7 together with the accompanying actuating voltages.

The maximum sensitivity in displacement measurements is 198.49 Hz/m. Given that a 1 mm thick diaphragm is deflected at the center for 1 m at 21 Bars, the sensitivity is 9.45 Hz/Bar.

7.3 Assembly of Device

Before gathering of the gadget, a board is ready for sensor to sit on. A little copper board with aspects 5.96 mm x 20 mm x 1.5 mm is cut for that reason. After electrical associations are made on the board, links are patched. There are 5 links emerging from the board 3 being drive, sense and confirmation mass associations and the leftover 2 being in the middle between. The ground terminals are intended to diminish impedance between drive, verification mass and sense signals. Then MEMS sensor is put. The contact among board and sensor is laid out by means of silver epoxy. Then electrical associations are taken out to the copper board from sensors

terminals. At long last, sensor is put in metal chamber which will squeeze into pressure port. An image of this first establishment is given in Figure 7.10. As of now tip arrangement is vital. Because of filets on the edge of stomach, tip needs to connect from the chamber for another 250 µm to guarantee its association with stomach. Comparing magnifying lens view should be visible in Figure 7.11.

Figure 7.10 - Close up view of a sensor inside the cylinder with its electrical connections completed.

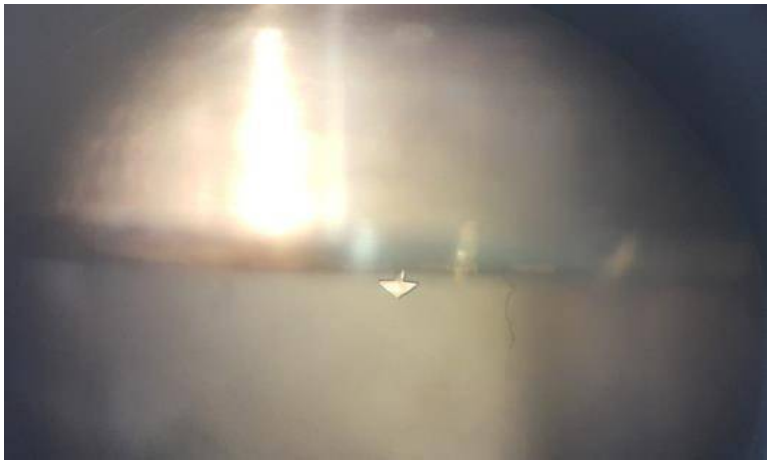

Figure 7.11 - Microscope view of tip left out of the cylinder. Approximately 250 µm of it is out asdesired.

After the board has been epoxy-fixed to the cylinder, it is surrounded by a pressure port and tested. When a 1 kHz change in its frequency response was noticed, it was eventually repaired with epoxy. This shift is seen in the image below.

Final view of the device is given in Figure 7.13.

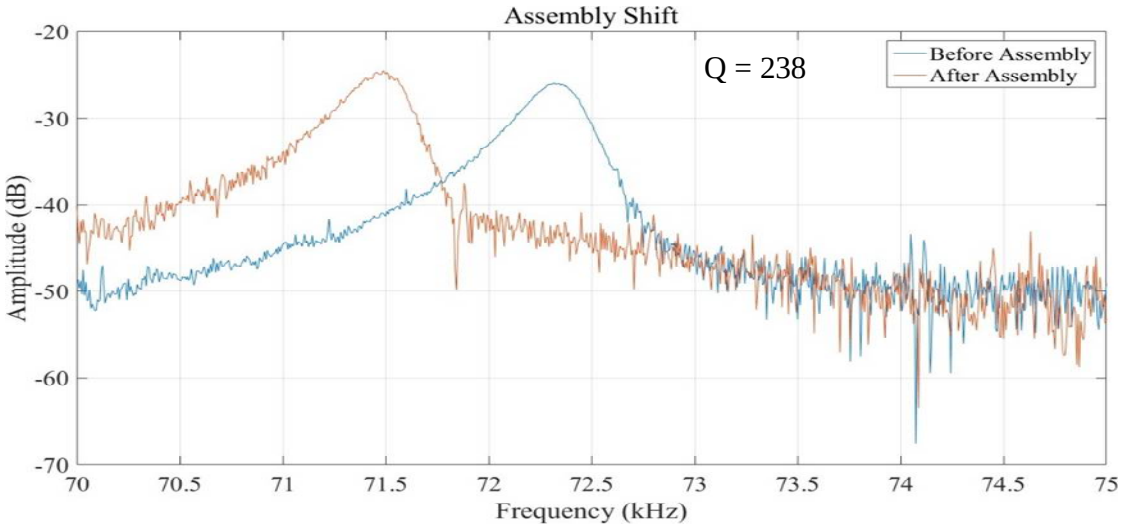

Figure 7.12 - Illustration of frequency shift occurred during assembly which ensures that tip is in contact.

Figure 7.13 - Assembled view of the hydraulic pressure sensor

7.4 Hydraulic Pressure Tests

Texas Instrument's minimal expense operation amp LF-353 is utilized all through reverberation tests. It ought to be referenced that this enhancer commotion properties are utilized in plan streamlining. Yet, solely after MEMS sensor is set onto a circuit board, this speaker became deficient with regards to its clamor properties. On the other hand, Texas Instrument's low commotion, surface mount operation amp which likewise has a more extensive band, OPA-656 is utilized. Trans-impedance enhancer circuit for OPA-656 requires a smidgen change as it need capacitances between power pins for activity. Because of Mustafa Kangul, this circuit was promptly accessible for use and straightforwardly embraced.

Water driven pressure tests are led at METU Mechanical Engineering Department Automotive Laboratory. Image of the arrangement is displayed in Figure 5.14. Strung part of tension port is planned to fit the water powered hardware in the lab. Test gear can apply a strain of 50 Bars with misfortunes included. The tension qualities are estimated ahead of time at a similar place where the gadget is put to be precise.

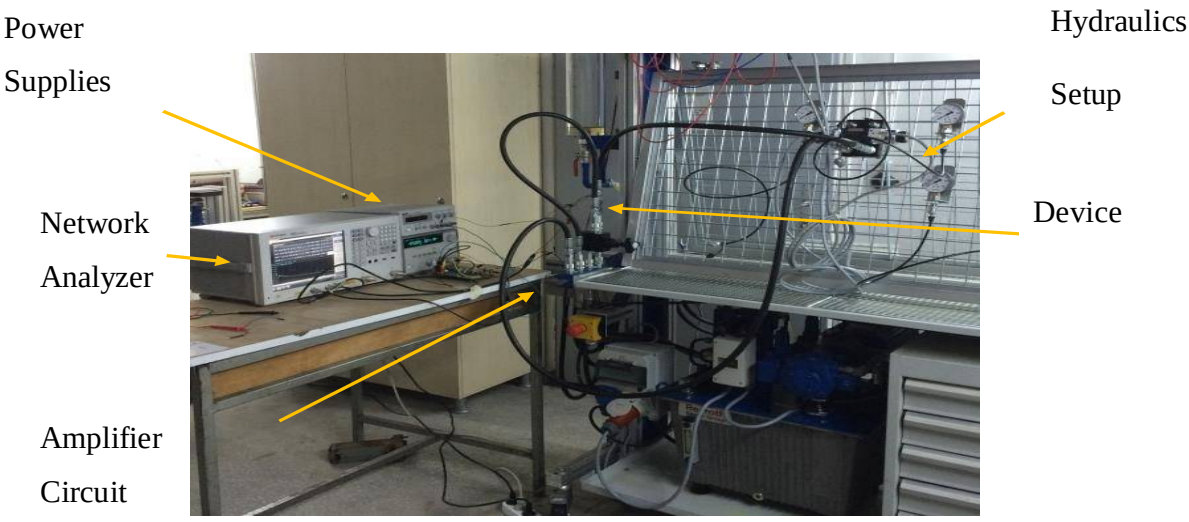

Figure 7.14 - Picture of hydraulic pressure test setup

Tests information is gathered for 5 strains face up to 50 Bars. This time reverberation top can't rule clamor level well. There are 2 primary reasons of this. In the first place, test are completed with a proof mass voltage of 15 and 24 V. Recalling that the past tests were directed with 40 V, a more modest reverberation tops are normal. Also, dynamic test which was accessible for uprooting tests were absent in the arrangement. At the point when a functioning test is used for the sending yield voltage sign to the framework, reverberation tops are very much noticed and clamor level is stifled. Recurrence reaction of the gadget at applied pressure scope of 0 - 50 Bars is shown in following figures. 6 reactions which have a place with 6 distinct data of interest, are given independently on the grounds that it tends to be truly challenging to break down them in a single figure due to commotion level.

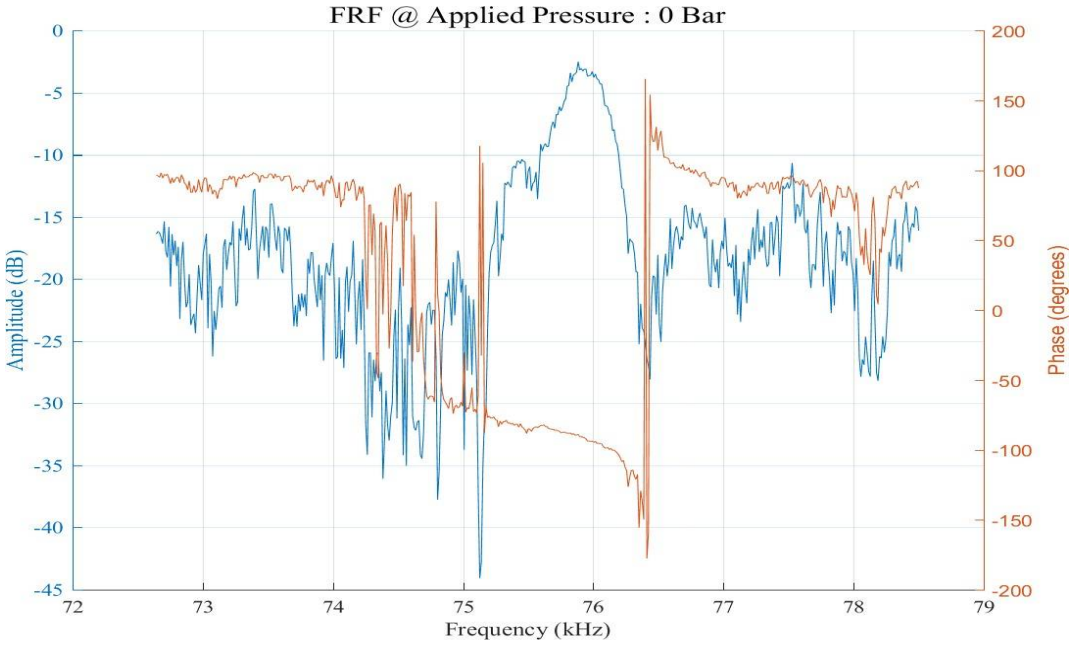

Figure 7.15 - Frequency response of the device with no applied pressure

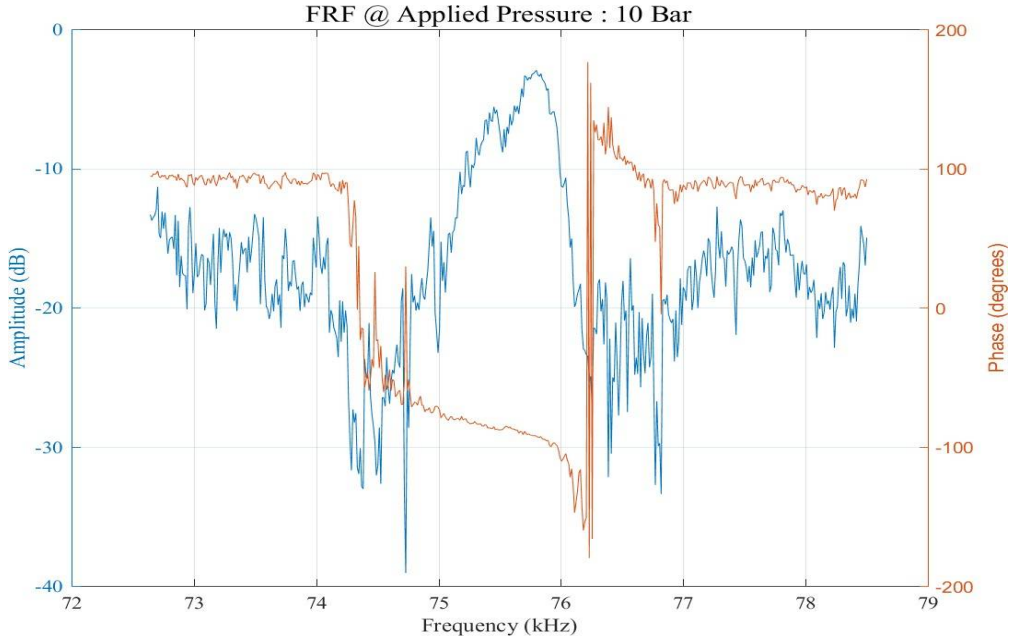

Figure 7.16 - Frequency response of the device at 10 Bars of applied pressure

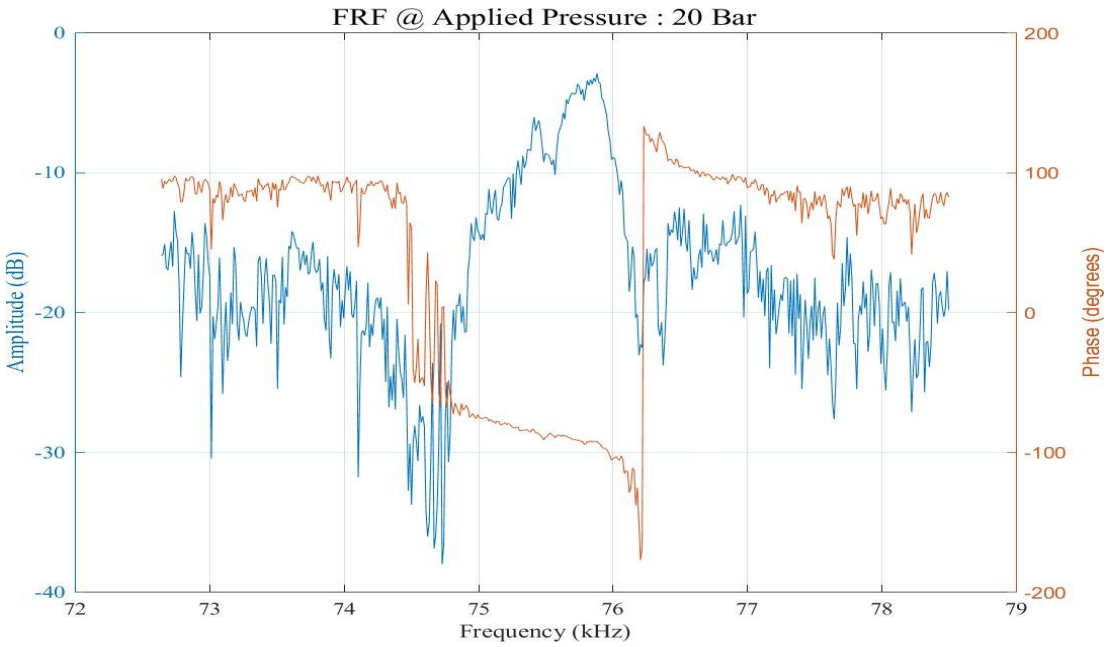

Figure 7.17 - Frequency response of the device at 20 Bars of applied pressure

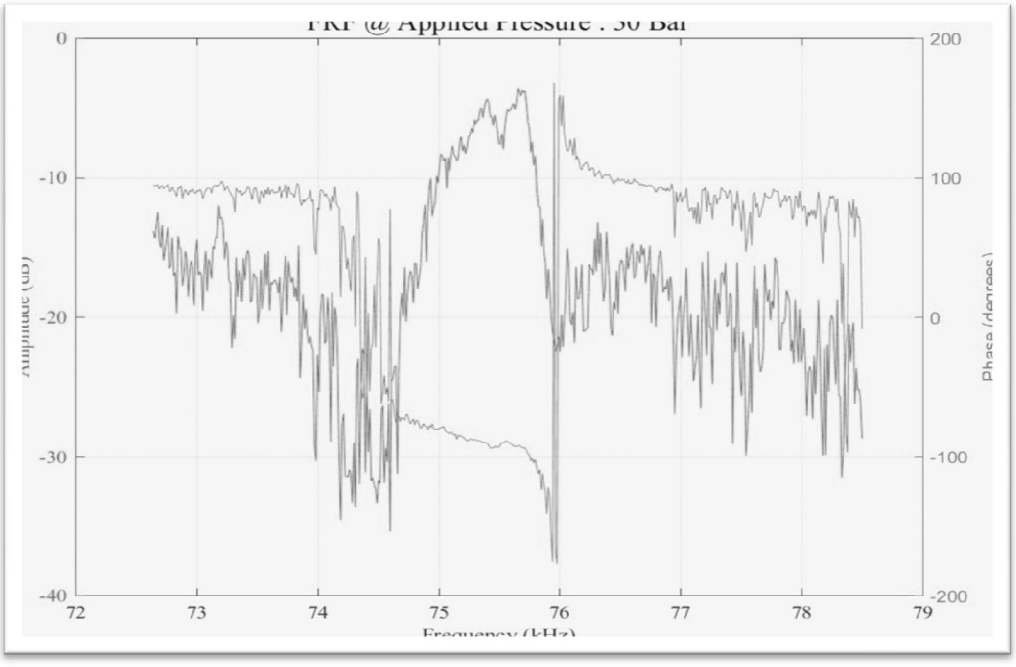

Figure 7.18 - Frequency response of the device at 30 Bars of applied pressure

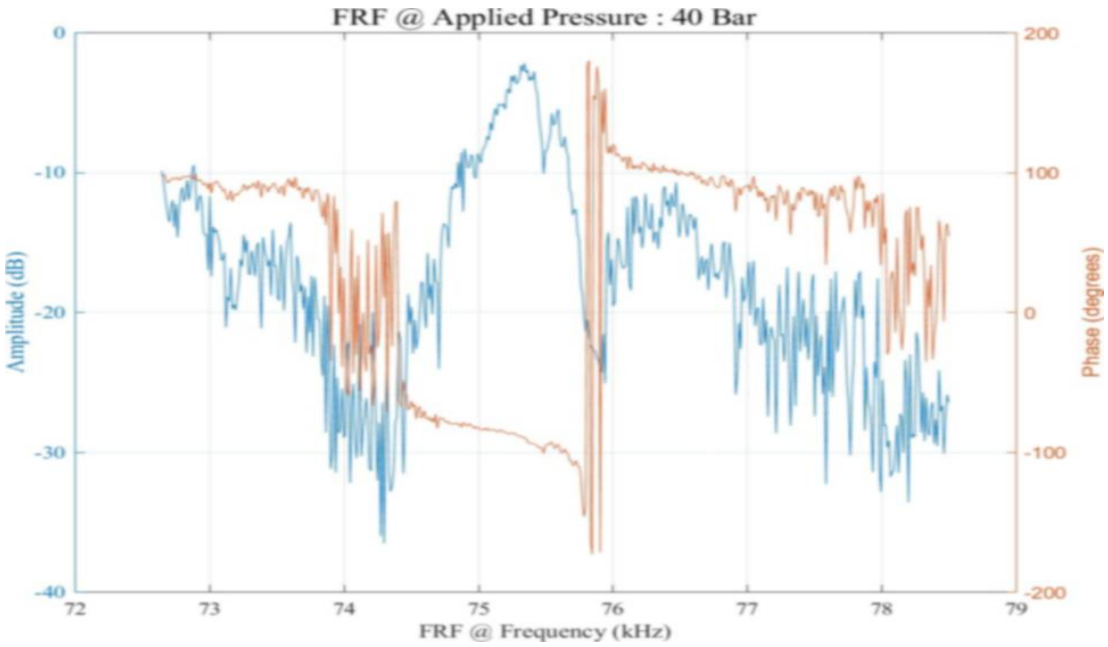

Figure 7.19 - Frequency response of the device at 40 Bars of applied pressure

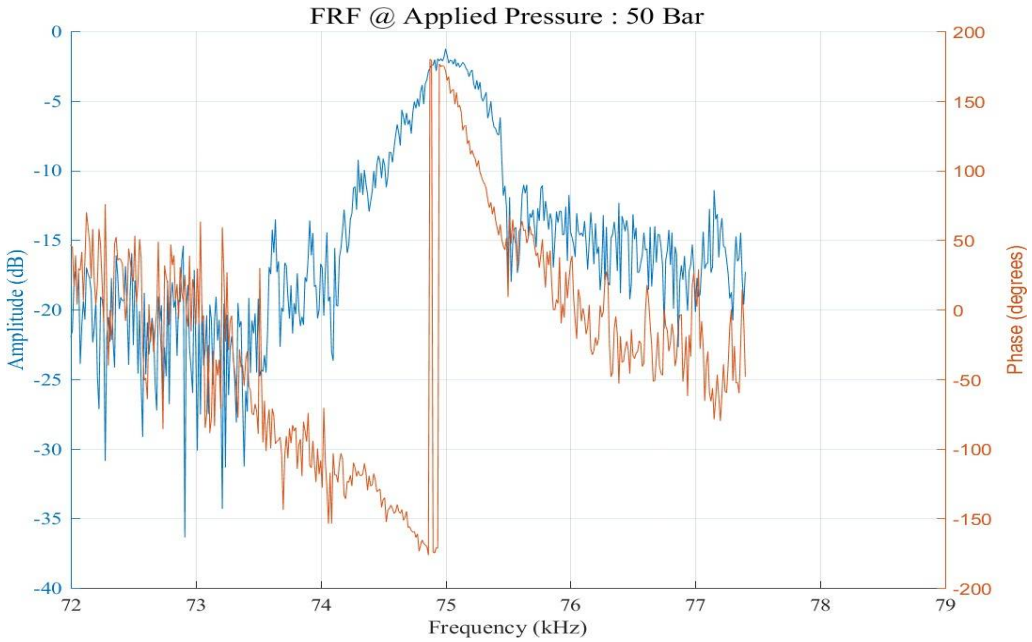

Figure 7. 20 - Frequency response of the device at 50 Bars of applied pressure

In pressure testing, an 884 Hz frequency shift is detected for 50 Bars of hydraulic pressure application, corresponding to calculated pressure sensitivity of 17.68 Hz/Bar. As predicted, the minimum and maximum sensitivities are achieved at 0-10 Bars and 40-50 Bars, respectively, with corresponding values of 5 Hz/Bar and 34.40 Hz/Bar. Figure 5.1 illustrates the collated findings.

Table 7.1 - Natural frequencies extracted from Figure 7.15 - 20 by curve fitting

Pressure	Natural Frequency
0Bars	75928.2kHz
10Bars	75794.0kHz
20Bars	75845.3kHz
30Bars	75652.2kHz
40Bars	75355.0kHz
50Bars	75021.7kHz

Remember that displacement experiments revealed a maximum sensitivity of 9.45 Hz/Bar. The disparity is mostly due to the fact that the displacement universal testing machine, as well as the sensor itself, cannot be entirely repaired. As the piezoelectric actuator pushes the sensor, both of them move somewhat, causing the sensitivity to be recorded incorrectly. However, because the sensor is securely mounted within the device, the sensitivity is measured more precisely.
As previously stated, noise-affected reaction is likewise to be expected. This may be avoided by modifying the design to increase the quality factor and output voltage.
Finally, the hydraulic pressure vs natural frequency curve is depicted in the image below,

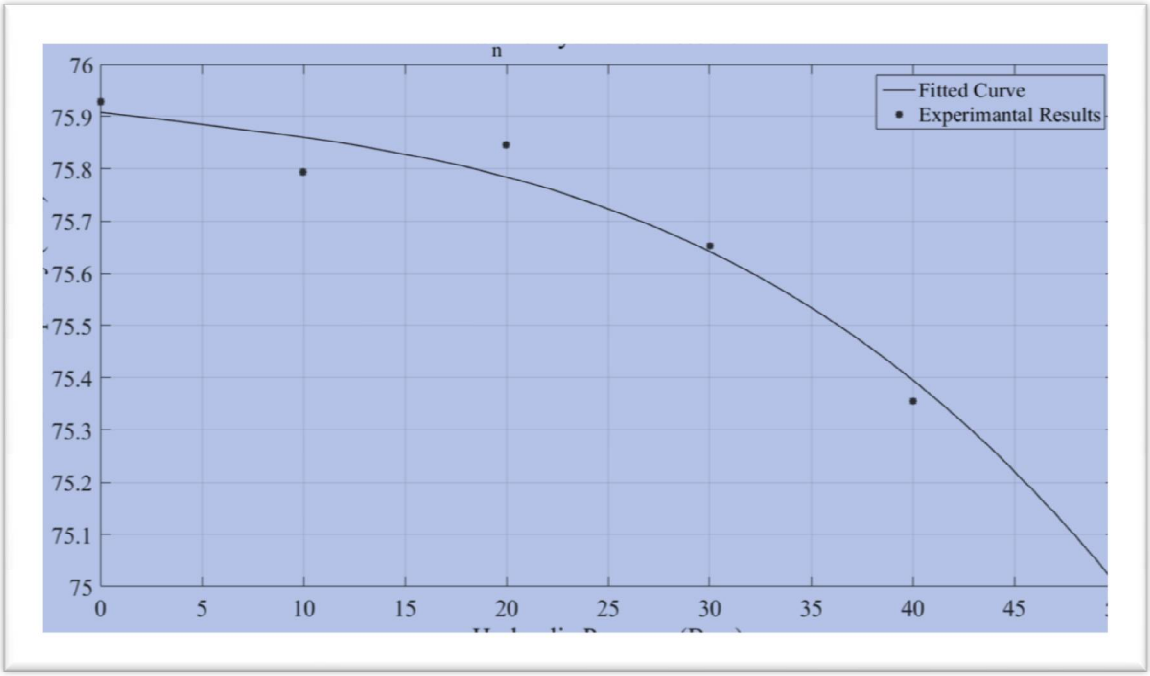

Figure 7.21 - Natural frequency vs hydraulic pressure data given with 3rd order polynomial fit.

The highest absolute inaccuracy for this curve in the information gathered is 66 Hz. It is an extremely big inaccuracy, most likely caused by a measurement error.These results of tests on devices with improved geometry are shown. Along with these findings, the detector configuration and sensor assembly with pressure port are detailed. There are three sorts of tests. The functional devices are first identified and separated using resonance measurements. The resonance tests are carried out using the probe station without the need of any wire. Second, displacement testing using operational devices are carried out utilizing a precision piezoelectric actuator**.** These experimental results simulate a misalignment of around 120 m, and the resulting data is presented. As a result, the anticipated frequency shift is demonstrated. In the third step of testing, a MEMS sensor is combined with a pressure port to detect the center deflection of the diaphragm when hydraulic pressure is applied. It shows the constructed device's frequency response at six distinct data points between 0 and 50 bars. Finally, a fitted curve is used to link applied hydraulic pressure to natural frequency, and its expression is presented

CHAPTER 8

CONCLUSIONS

The design and functioning of a MEMS-based resonant hydraulic pressure sensor are demonstrated. The dissertation proposes a novel technique for identifying pressures using only a tuning fork resonator, which may lead to enhanced concentration of the sample in the future. For the time being, it has been proved effectively that an extremely sensitive tuning fork tip may be used in an orthogonal orientation to the diaphragm.

Although the device's sensitivity is not currently as high as that of its competitors, this can be substantially improved in the future. It is possible to employ a stiffer spring element. The device's tip would thus deflect more under unit pressure. Before the device was assembled, it was anticipated that a deflection capacity of 100 m would enough; nevertheless, it appears that this is more than adequate. The tip is not shattered as a result of the sensor's own bulk. Even the extra weight of the circuit board is tolerable. As a result, the sensor may be conveniently mounted in the combustor of something like the pressure gauge in vertical form. The sole requirement is a finely machined diaphragm surface, which is also possible with superior milling tools.

Future research might modify the building's mathematical framework to control two masses, which is more suitable for capacitive plates with various intervals. Because it takes into account the rigidity of the plates, this approach provides a more realistic result.

Temperature adjustment should also be incorporated to the device since, during testing, the temperature of the hydraulic pressure setup rises significantly. Given that silicon has a Young's Modulus temperature coefficient of -60 ppm/K [36], the resonance frequency only changes with temperature, which might lead to incorrect interpretation of the detected domain.

Normal recurrence of the gadget was altogether different than single level of opportunity model. Yet, this was normal as a result of long capacitive plates which are thought to be inflexible. The regular recurrence of the gadget was found as 79.48 kHz after expansion of

spring and roller structure. Nonetheless, microfabricated gadgets has a characteristic recurrence around 71.5 kHz. This can be made sense of by leftover burdens which may currently introduce in the wafer and undercut. It's a good idea that lingering pressure is successful in light of the fact that the activity rule of sensor depends back to utilization of stacking, which causes pressure, which causes recurrence change. Additionally undercut in creation steps diminishes the solidness more than it diminishes mass, since length of the prongs stays consistent while the width diminishes. As an outcome, normal recurrence is digressed from anticipated by 10 %. Yet, this changed the assumption for different properties like quality element too. For instance, FEM model tracks down width of one prong as 14.7 µm for the improved plan aspects to have a characteristic recurrence of 71.5 kHz. At the point when this worth is embedded into scientific model for assessing quality element, the resultant quality component is gotten as 273. Recalling that streamlining routine tracks down quality variable as 339 without the impacts of undermined, quality component assessment of 273 is 15 % nearer to estimated esteem with 14 % exactness.

In the writing quality elements of 1800 are reached with DETF resonators which have brush fingers [20]. The responsiveness of an optical MEMS water powered pressure sensor which has 200 bars estimation range is accounted for in the writing with an awareness of 13.17 Hz/Bar [10]. For a smaller scope of 4 bars 2014 Hz/Bar of responsiveness is likewise present [20]. For the proposed sensor, responsiveness and quality element is liable to increment after couple of adjustments on the math. Eliminating spring component from the construction, first of all, could expand the responsiveness multiple times which is left as a future work. Additionally, stomach which is machined with appropriate hardware to have ideal thickness would increase the awareness by 1.5. Hence 17.68 Hz/Bar responsiveness guarantee a great deal for what's in store. Also, with a slight change on the brush finger length quality element of the gadgets can be supported up to 2500 in principle.

Fabrication must also be much improved throughout this procedure. However, a very easy and useful proposal for fabrication is to utilize the fourth photolithography mask as the first, i.e. manufacturing may have begun with handle layer oxide patterning and continued from the first mask. This is mostly due to the challenge and complexity of designing the reverse whereas the device layer silicon is patterned and etched. If, on the other hand, the process

begins with the fourth mask, there is no need to link either semiconductor to SOI.

Another aspect of the design that is lacking is tip protection. Devices have extremely fragile tips that can be harmed by the smallest error. While a semiconductor capping layer would be highly successful in shielding the tip from unintentional out-of-plane loads, the tip might have at least been concealed within in the device, enabling just 100 m at the outside for deflection. During testing, this would have averted at least half of the mishaps that resulted in equipment loss.

Self-resonance circuitry with feedthrough cancellation may be applied to gadgets as future research. Since the quality factor is low, stray capacitances cannot be effectively controlled by resonance peak without secondary complications elimination. As a result, when both are used, resonance may be maintained. This would also open the way for measuring the sensor's resolution.

REFERENCES

[1] K. E. Petersen, "Silicon as a mechanical material," *Proceedings of the IEEE*, vol.70,pp. 420-457, 1982.

[2] G.-C. Manuel and H. Vlad, "Using a Torsional Balance to Characterize Thrust atMicroNewtonLevels,"in*39thAIAA/ASME/SAE/ASEEJointPropulsionConference and Exhibit*, ed: American Institute of Aeronautics and Astronautics,2003.

[3] K. Bongsang, R. N. Candler, M. Hopcroft, M. Agarwal, P. Woo-Tae, and T. W.Kenny, "Frequency stability of wafer-scale encapsulated MEMS resonators," in*Solid-StateSensors,ActuatorsandMicrosystems,2005.DigestofTechnicalPapers. TRANSDUCERS '05. The 13th International Conference on*, 2005, pp.1965-1968 Vol.2.

[4] M. Strano, "Optimization under uncertainty of sheet-metal-forming processes bythefiniteelementmethod,"*ProceedingsoftheInstitutionofMechanicalEngineers, PartB:JournalofEngineeringManufacture*,vol.220,pp.1305-1315,2006.

[5] P. Ray and B. J. Mac Donald, "Determination of the optimal load path for tubehydroforming processes using a fuzzy load control algorithm and finite elementanalysis,"*FiniteElementsinAnalysisandDesign*,vol.41,pp.173-192,11//2004.

[6] J. Paros, E. Bernard, J. Delaney, C. Meinig, M. Spillane, P. Migliacio, *et al.*,"Breakthrough underwater technology holds promise for improved local tsunamiwarnings," in *Underwater Technology (UT), 2011 IEEE Symposium on and 2011WorkshoponScientificUseofSubmarineCablesandRelatedTechnologies(SSC)*, 2011, pp.1-9.

[7] H. Matsumoto, E. Araki, and K. Kawaguchi, "Initial characteristics of pressuresensors,"in*Underwater Technology (UT), 2015 IEEE*,2015, pp. 1-5.

[8] A. J. Trujillo, B. Guamis, and C. Carretero, "A procedure for the manufacture ofgoatmilkcheesewithcontrolled-microflorabymeansofhighhydrostaticpressure,"*Food Chemistry,* vol. 69, pp. 73-79, 4// 2000.

[9] X. Ma, "Research on the best autofrettage pressure of ultra-high pressure valvebody,"in *KeyEngineering Materials*vol. 667, ed,2016, pp. 524-529.

[10] W.Challener,S.Palit, R.Jones,L.Airey,R.Craddock,andA.Knobloch,"MOEMS pressure sensors for geothermal well monitoring," 2013, pp. 861603-861603-12.

[11] G. Fragiacomo, K. Reck, L. Lorenzen, and E. Thomsen, "Novel Designs forApplicationSpecific MEMSPressureSensors,"*Sensors,*vol. 10, p.9541, 2010.

[12] H. I. Kuo and W. H. Ko, "Smart-cut™ piezoresistive strain sensors for hightemperatureapplications,"in *ProceedingsofIEEESensors*,2009,pp.1290-1292.

[13] M. Rajavelu, D. Sivakumar, J. Daniel Rathnam, and K. Sumangala, "Enhancedsensitivity withextendedlinearity inMEMSpiezoresistivepressuresensor,"*Microand Nano Letters,*vol. 8, pp. 753-756, 2013.

[14] P.K.KinnellandR.Craddock,"AdvancesinSiliconResonantPressureTransducers,"*P rocediaChemistry*,vol. 1, pp.104-107, 9// 2009.

[15] Z.Dibi,A.Boukabache,andP.Pons,"Combinedeffectofthemembraneflatnessdefect and real dimensions gauges on the sensitivity of a silicon piezoresistivepressuresensor,"in*Proceedings ofIEEE Sensors*,2002, pp. 990-993.

[16] A.CheshmehdoostandB.E.Jones,"Designandperformancecharacteristicsofanintegr ated high-capacity DETF-based force sensor," *Sensors and Actuators A:Physical*,vol. 52, pp. 99-102, 3// 1996.

[17] K. Petersen, F. Pourahmadi, J. Brown, P. Parsons, M. Skinner, and J. Tudor,"Resonantbeampressuresensorfabricatedwithsiliconfusionbonding,"in*Solid -State Sensors and Actuators, 1991. Digest of Technical Papers, TRANSDUCERS'91.,1991 InternationalConferenceon*, 1991, pp.664-667.

[18] K.AzginandL.Valdevit,"Theeffectsoftinecouplingandgeometricalimperfections on the response of DETF resonators," *Journal of MicromechanicsandMicroengineering*,vol. 23, p. 125011, 2013.

[19] M.A.SchmidtandR.T.Howe,"SiliconResonantMicrosensors,"in*14thAutomotiveMaterialsConference:CeramicEngineeringandScienceProceedings*,ed: John Wiley&Sons,Inc., 2008,pp. 1019-1034.

[20] S. Ren, W. Yuan, D. Qiao, J. Deng, and X. Sun, "A Micromachined PressureSensor with Integrated Resonator Operating at Atmospheric Pressure," *Sensors*,vol. 13, p. 17006, 2013.

[21] C. J. Welham, J. Greenwood, and M. M. Bertioli, "A high accuracy resonantpressure sensor by fusion bonding and trench etching," *Sensors and Actuators A:Physical*,vol. 76, pp. 298-304, 8/30/ 1999.

[22] D.Chen,Y.Li,M.Liu,andJ.Wang,"Designandexperimentofalaterallydrivenmicromachined resonant pressure sensor for barometers," *Procedia Engineering*,vol. 5, pp. 1490-1493, // 2010.

[23] B.Xie,Y.Xing,Y.Wang,J.Chen,D.Chen,andJ.Wang,"ALateralDifferentialResonantPressureMicrosensorBasedonSOI-GlassWafer-LevelVacuumPackaging,"*Sensors,* vol. 15, p. 24257, 2015.

[24] M. H. Houston and J. M. Paros, "High accuracy pressure instrumentation forunderwater applications," in *Underwater Technology, 1998. Proceedings of the1998International Symposium on*, 1998, pp. 307-311.

[25] X. Zhou, T. Jiang, J. Zhang, X. Wang, and Z. Zhu, "Humidity sensor based onquartz tuning fork coated with sol–gel-derived nanocrystalline zinc oxide thinfilm,"*Sensors and Actuators B:Chemical*,vol. 123, pp.299-305, 4/10/ 2007.

[26] R. G. Hennessy, M. M. Shulaker, M. Messana, A. B. Graham, N. Klejwa, J.Provine, *et al.*, "Vacuum encapsulated resonators for humidity measurement,"*Sensorsand Actuators B: Chemical*,vol. 185, pp. 575-581, 8//2013.

[27] P. Thiruvenkatanathan, J. Yan, and A. A. Seshia, "Ultrasensitive mode-localizedmicromechanical electrometer," in *Frequency Control Symposium (FCS), 2010IEEEInternational*, 2010, pp. 91-96.

[28] E. J. Ng, L. Hyung Kyu, C. H. Ahn, R. Melamud, and T. W. Kenny, "Stabilitymeasurements of silicon MEMS resonant thermometers," in *Sensors, 2011 IEEE*,2011,pp. 1257-1260.

[29] D. R. Myers and A. P. Pisano, "Torque measurements of an automotive halfshaftutilizingaMEMSresonantstraingauge,"in*TRANSDUCERS2009-15thInternational Conference on Solid-State Sensors, Actuators and Microsystems*,2009,pp. 1726-1729.

[30] M.W.Chan,D.R.Myers,B.D.Sosnowchik,L.Lin,andA.P.Pisano,"Localizedstrainsensing using highspatialresolution,highly-sensitive MEMSresonantstraingaugesforfailureprevention,"in*201116thInternationalSolid-StateSensors, Actuators and Microsystems Conference, TRANSDUCERS'11*, 2011, pp.2859-2862.

[31] S.X.P.Su,H.S.Yang,andA.M.Agogino,"Aresonantaccelerometerwithtwo-stage microleverage mechanisms fabricated by SOI-MEMS technology," *SensorsJournal,IEEE*,vol. 5, pp. 1214-1223, 2005.

[32] X. Zou, P. Thiruvenkatanathan, and A. A. Seshia, "A high-resolution micro-electro-mechanical resonant tilt sensor," *Sensors and Actuators, A: Physical*, vol.220,pp. 168-177, 2014.

[33] W. Zhang andJ. E. Y.Lee,"Frequency-basedmagnetic field sensing usingLorentzforceaxialstrainmodulationinadouble-endedtuningfork,"*SensorsandActuatorsA: Physical*,vol. 211, pp. 145-152, 5/1/ 2014.

[34] K. Azgin, T. Akin, and L. Valdevit, "Ultrahigh-dynamic-range resonant MEMSload cells for micromechanical test frames," *Journal of MicroelectromechanicalSystems*,vol. 21, pp. 1519-1529, 2012.

[35] S.Fan,L.Wang,andZ.Guo,"Anovelmicro-electromechanicalresonantgyroscope,"2008, pp. 71270D-71270D-7.

[36] M. A. Hopcroft, W. D. Nix, and T. W. Kenny, "What is the Young's Modulus ofSilicon?," *Microelectromechanical Systems, Journal of*, vol. 19, pp. 229-238,2010.

[37] W.Wang,J.Jia,andJ.Li,"Slidefilmdampinginmicroelectromechanicalsystemdevices,"*ProceedingsoftheInstitutionofMechanicalEngineers,PartN:JournalofNanoengineering and Nanosystems*,vol. 227, pp.162-170, 2013.

[38] Z.XiaandW.C.Tang,"Viscousairdampinginlaterallydrivenmicroresonators,"in*MicroElectro MechanicalSystems,1994,MEMS'94,Proceedings,IEEEWorkshopon*, 1994, pp.199-204.

[39] A. Torrents, K. Azgin, S. W. Godfrey, E. S. Topalli, T. Akin, and L. Valdevit,"MEMSresonantloadcellsformicro-mechanicaltestframes:feasibilitystudyandoptimal design," *Journal of Micromechanics and Microengineering*, vol. 20, p.125004, 2010.

[40] S.TimoshenkoandS.Woinowsky-Krieger,*Theoryofplatesandshells*:McGraw-Hill, 1959.

International Journal of All Research Education & Scientific Methods

UGC Certified Peer-Reviewed Refereed Multi-disciplinary Journal
ISSN: 2455-6211, New Delhi, India
Impact Factor: 7.429, SJR: 2.28, UGC Journal No. : 7647

Acceptance Letter

Dated: 23/06/2022

Dear Authors,

We are glad to inform you that your paper has been accepted as per our fast peer review process:

Authors Name: **Mr yaqoob Ali Ansari**

Paper Title: **Customization Of Mems Based Hydraulic Pressure Sensor**

Paper Status: **Accepted**

Paper Id: **IJ-2306221044**

for possible publication in **International Journal of All Research Education & Scientific Methods, (IJARESM), ISSN No: 2455-6211", Impact Factor : 7.429**,

in the current Issue, **Volume 10, Issue 6, June - 2022**.

Kindly send us the payment receipt and filled copyright form asap. Your paper will be published soon after your payment confirmation.

Best Regards,

Editor-in-Chief,
IJARESM Publication, India
An ISO & UGC Certified Journal
http://www.ijaresm.com